

(NASA-CR-157256) EXPERIMENTS ON THE  
STABILITY AND TRANSITION OF TWO-DIMENSIONAL  
AND THREE-DIMENSIONAL BOUNDARY LAYERS WITH  
SUCTION Final Report (Virginia Polytechnic  
Inst. and State Univ.) 71 p HC A04/MP A01

N79-27464

G3/34 Unclas  
29360

FINAL REPORT

NASA GRANT NSG-1358

Experiments on the Stability and Transition of  
Two-Dimensional and Three-Dimensional Boundary Layers with Suction

July 1979

by

William S. Saric\*

and

Gregory A. Reynolds\*\*

Department of Engineering Science and Mechanics  
Virginia Polytechnic Institute and State University  
Blacksburg, Virginia 24061

\*Professor, Principal Investigator

\*\*Graduate Research Assistant



## Abstract

This report contains the preliminary experimental development work directed towards the understanding of transition in boundary layers with suction. The work performed under this task extended only to the establishment of the basic stability experiment and the certification of the facility. The experiments with suction will be carried out in another task.

## TABLE OF CONTENTS

	<u>PAGE</u>
TABLE OF CONTENTS .....	ii
CHAPTER 1. INTRODUCTION.....	1
CHAPTER 2. WIND TUNNEL FACILITY AND EXPERIMENTAL APPARATUS.....	6
2.1 The Wind Tunnel Facility.....	6
2.2 The Model.....	8
2.3 Vibrating Ribbon.....	11
2.4 Traversing Mechanism and Test Section Configuration...	12
2.5 Hot-Wire Sting.....	14
2.6 Fixed Probe Mount.....	15
CHAPTER 3. EXPERIMENTAL PROCEDURES AND RESULTS.....	17
3.1 Basic Measuring Devices and Instrumentation.....	17
3.2 Mean Flow Measurements.....	18
3.3 Boundary-Layer Stability Measurements.....	22
CHAPTER 4. CONCLUDING REMARKS.....	30
REFERENCES.....	33
APPENDIX.....	35
FIGURES.....	38

## CHAPTER 1

### INTRODUCTION

The process of transition from a laminar to a turbulent boundary layer is a frequently encountered phenomenon when considering fluid flow past a body. Due to the complexity of this nonuniform and unsteady process, a concise description of transition is far from complete.

The idea that small disturbances present in a laminar boundary layer may eventually lead to transition was proposed by Tollmien (1929) and Schlichting (1933). Experiments conducted by Schubauer and Skramstad (1947) showed that transition was a strong function of the natural disturbances present in the free stream. In doing so, they were the first to document the presence and growth of sinusoidal velocity fluctuations, or Tollmien-Schlichting (T-S) waves, in a laminar boundary layer. Continued work in the area of laminar boundary-layer stability has been motivated by the substantially lower skin friction and heat transfer for laminar layers as compared with turbulent layers. Drag reduction is of great practical significance, particularly in increasing the fuel efficiency of aircraft by delaying transition using laminar flow control (LFC). Previous research, including full-scale flight tests with the X-21 program, has demonstrated that LFC can be achieved under some conditions.

Laminar flow control on aircraft is primarily an attempt to maintain laminar boundary layers on the wings, thereby reducing the friction drag on the wings to as much as a fifth of its corresponding turbulent

value. The most promising method of achieving LFC involves the use of boundary-layer suction which has been accomplished with the use of distributed suction slots. The use of a porous surface material has also been proposed.

Although there exists experimental evidence of the feasibility of LFC and computational methods exist to predict the boundary-layer stability characteristics, further experimental work is needed. Additional experimental evidence will add to the fundamental knowledge of the transition process as well as substantiate the existing theoretical models which serve as a basis for aircraft design capabilities. The experiments developed here at VPI & SU have been designed with these needs in mind. The objective of this experimental program is a detailed study of boundary-layer stability and transition processes with and without LFC. These experiments will eventually be performed for flow past curved surfaces and three-dimensional swept-wing models.

The work described in this report was the first stage of this program; that is the development of the experimental capabilities to investigate the stability of a laminar boundary layer on a flat plate with zero chordwise pressure gradient. This type of experiment, first conducted by Schubauer and Skramstad (1947) and later by Ross et al (1970), Kachanov et al (1975), and Strazisar et al (1975), serves as the foundation for the more involved experiments. Thus the base state of the experiment is established by comparison with existing data.

The methods for investigating the behavior of T-S waves in the boundary layer were basically like those used by previous investigators. Periodic disturbances of known frequency were introduced into the bound-

ary layer by means of a vibrating ribbon. The vibrating ribbon created fluctuating velocity components,  $u$  and  $v$  in the  $x$  and  $y$  directions respectively, which were superposed on the mean boundary-layer velocity. In this case the  $x$ -direction is parallel to the flow and the  $y$ -direction is normal to the surface. A few boundary-layer thicknesses downstream of the vibrating ribbon the fluctuating disturbance components established themselves across the boundary layer into a regular pattern as shown in Figure 1.1. With the use of a hot-wire anemometer, the distribution of the r.m.s. disturbance velocity,  $|u|$ , through the boundary layer was measured. The change in the maximum disturbance amplitude (located at  $\eta = \eta_c$ ) was measured in the streamwise direction.

A typical result of this type of measurement is shown in Figure 1.2. The points  $R_I$  and  $R_{II}$ , where  $du_{III}/dx = 0$ , are called neutrally stable points and are identified with a Reynolds number based on the thickness  $\delta_r = (\nu x/U_\infty)^{1/2}$ . The locus of points  $R_I$  and  $R_{II}$  as a function of the dimensionless frequency,  $F = (fv/U_\infty^2)$ , of the disturbance is the neutral stability curve presented in Figure 1.3. Between branch I and branch II the amplitude is growing and this is an unstable region. The lowest value of  $R_I$  found for all frequencies is the critical Reynolds number.

The results of the linear stability theory applied to laminar boundary-layer disturbances are also shown in Figure 1.3. Until recently, the linear stability theories considered the boundary-layer flow as being parallel. These models did not account for the growth of the boundary layer in the streamwise direction and hence did not fully agree

with the experimental evidence. Recently however, linear stability theories which account for nonparallel-flow effects (Bouthier, 1973; Nayfeh, Saric, & Mook, 1974; Gaster, 1974; Saric & Nayfeh, 1975) have shown much better agreement with experiment as illustrated in Figure 1.3.

These linear models are valid when the velocity fluctuations in the boundary layer are small. In this case, the wave behavior is described by an eigenvalue problem and so it is not dependent on the disturbance amplitude. However, when the disturbances become large, the linear models no longer hold. For large amplitude waves, nonlinear interactions are likely, resulting in an exchange of energy between waves of different frequencies (Kachanov et al, 1977, 1978). This type of behavior is very amplitude dependent and must be explained by nonlinear models. Recently, nonlinear models have been developed to predict two and three wave interactions (e.g., Nayfeh & Bozatti, 1978).

Further experiments on nonlinear boundary-layer stability are currently being conducted at VPI & SU using the experimental apparatus described here. These experiments were motivated by the need for information leading to an understanding of the nonlinear interactions of T-S waves before the occurrence of transition as well as for knowledge of the influence of initial disturbance amplitudes on transition. Future experiments will be conducted on a flat plate model with suction in order to determine the influence of LFC on the nonlinear behavior of T-S waves. These experiments can then be carried one step further to investigate these phenomena on three-dimensional surfaces.

The development of the flat plate experiments without suction is the topic of this report. The experimental apparatus is described in Chapter 2 and a description of the wind tunnel facility and its capabilities for boundary-layer stability experiments are included. The flat plate model and traversing mechanism are also described in this chapter. The experimental methods and the results of measurements to determine the flow quality are presented in Chapter 3. In the remainder of Chapter 3 the preliminary measurements of neutrally stable T-S waves are given. Remarks on the current state of the experiments and recommendations are found in Chapter 4. A detailed description of the instrumentation employed in the experiments is located in the Appendix.



## CHAPTER 2

### WIND TUNNEL FACILITY AND EXPERIMENTAL APPARATUS

#### 2.1 The Wind Tunnel Facility

The experiments were performed in the VPI & SU Stability Wind Tunnel. This wind tunnel was originally a NACA facility located at Langley Field in Hampton Virginia. Constructed in 1940, the facility was designed to provide a very low-turbulence level flow for conducting dynamic stability measurements. The wind tunnel was moved to VPI & SU and reconstructed in 1958. Present studies revealed that the facility had very good flow quality, even when compared with present-day designs. For boundary-layer experiments, extremely low free-stream turbulence levels were necessary. These levels were found to be in the range of .02%-.04% of the free-stream velocity. Moreover, the spectrum of the disturbances showed most of the energy below 20 Hz. The flow quality is discussed in more detail in Chapter 3.

The facility was a closed loop with an air-exchange tower which was open to the atmosphere. A plan view of the facility is shown in Figure 2.1. The tunnel circuit had no heat exchanger for temperature control, however temperature stability was maintained by partial air replacement via the air-exchange tower. The air-exchange tower was located downstream of the fan and motor assembly and used a boundary-layer bleed on the entry flow. Turning vanes were located at each corner of the tunnel circuit in order to maintain uniform flow. The relatively low air

velocities in the settling chamber and through the turbulence screens allowed large scale turbulent eddies to be dissipated.

The seven turbulence screens were 30 mesh screens of 0.2 mm diameter stainless steel wire. The screen open-area ratio was 0.6. Experiments were performed to determine optimum damping screen mesh size (Bradshaw 1965), and based on this work, it was suggested that screens having an open-area ratio greater than 0.57 can be used for boundary-layer measurements. The damping screens in the VPI & SU facility were found to be quite effective in reducing the turbulence level and did not appear to generate spanwise mean-flow fluctuations on the model. The 5.5 m square screen panels were constructed from three 1.83 m x 5.5 m screens joined together. The two seams in each screen panel were approximately 2 mm wide. The screen panel furthest downstream had horizontal seams and alternate upstream panels were rotated 90°. This resulted in four horizontal and three vertical sets of seams. A check of variations in the freestream turbulence levels in the test section revealed that any turbulence being shed from the screen seams was dissipated in the nozzle and did not reach the test section. The screens were drawn very tight and held by clamps around the inside perimeter of the settling chamber walls. The spacing between screens was 146 mm. The screen clamps were offset from the settling chamber wall, which resulted in a 25 mm space around the perimeter of the screens. Due to the screen blockage, a wall jet was created as the flow left the turbulence screens. Downstream of the turbulence screens the flow underwent a 9:1 area contraction ratio as it passed through the nozzle and into the test section. Flow visualization in the nozzle with string tufts as well as hot-wire measurements

in the boundary layer showed that the boundary layers were not unusually thick and there was no separation bubble in the nozzle. The test section was enclosed in an airtight control room. The control room was at the same static pressure as the test section and this minimized the problem of air leakage into the test section flow. The test section was 7.3 m long with a constant square cross section of 1.83 m. Since there was no allowance for growth of the wall boundary layers, a slight negative pressure gradient of approximately  $C_p = 0.3\%$  per meter was present.

The flow was driven by a 4.3 m dia. propeller that had eight constant pitch blades. Power for the fan was provided by a 450 kW, d.c. motor. This system was capable of providing stable free-stream velocities in the test section in the range of 4.6 m/s to 67 m/s. The fan motor assembly was mounted on an isolated foundation.

Electrical power for the d.c. motor was supplied by a Westinghouse Model No. 28767 motor-generator. The motor-generator was also mounted on its own foundation. However, the generator rotational speed of 900 r.p.m., or 15 Hz, was found to be a source of vibration in the test section.

## 2.2 The Model

The wind-tunnel model was a 1.83 m x 3.7 m flat plate constructed for these experiments by Brunswick Corporation in Marion, Virginia. The model was a laminated panel that consisted of a 19 mm paper honeycomb core sandwiched between two, 1 mm 6061-T6 aluminum sheets. The overall thickness of the panel was 21.6 mm. This design was chosen for its ease

of handling, light weight, strength, and very flat surfaces that were insensitive to temperature and humidity changes.

The mounting of a number of fixtures on the back of the plate was facilitated by thirty-four threaded inserts which were flush mounted and held in place by fiberglass potting resin. The leading edge and the electromagnets for the vibrating ribbon were mounted using the threaded inserts. Additional threaded inserts were located on the back of the plate to allow the mounting of vacuum manifolds so that the model could be adapted to experiments with boundary-layer suction. The threaded insert locations are shown in Figure 2.2.

A 0.34 m x 1.83m tapered leading edge was mounted onto the front of the plate which gave a total model length of 4.0 m. The leading edge had an elliptical profile with a ratio of major to minor axes of 67:1. This leading-edge profile was chosen to minimize the stagnation point pressure rise, and yet be insensitive to leading-edge separation at slight angles-of-attack.

The leading edge was fabricated at Dynamic Engineering in Newport News, Virginia. The elliptical profile was machined from a single piece of aluminum using a numerically controlled milling machine. Tolerances for the profile shape were  $\pm 0.03$  mm near the stagnation region and  $\pm 0.1$  mm near the flat-plate junction. A surface finish of  $8 \mu\text{m}$  was obtained by hand polishing. Four mounting brackets were epoxied to the notched area at the root of the leading edge. The brackets bolted directly to the back side of the plate with sixteen threaded inserts. At the leading edge-plate junction, the leading edge was parallel to the front surface of the plate. Due to the different thermal coefficients

of expansion of the two materials, a slight step or gap resulted at the junction. This step or gap was generally less than .02-.05 mm and was easily faired by using a polyester patching compound. Repair of the leading edge junction was usually necessary only when the seasons of the year changed which resulted in large temperature changes from the previous test series. The leading edge - flat plate junction is shown in Figure 2.3.

Static pressures on the test side of the plate were measured by 93 static pressure ports. A pressure port consisted of a 6.3 mm diameter cylindrical aluminum insert with an orifice at one end and a copper tube at the other end, as shown in Figure 2.4. This configuration permitted easy and reliable attachment of pressure tubing and provided static pressure measurements without disturbing the flow. The pressure port inserts were press-fit into holes in the flat plate and potted in place. This arrangement is shown in Figure 2.5. The 93 pressure ports shown in Figure 2.6 were located to provide the spanwise and chordwise pressure measurements. With the pressure ports installed, surface irregularities were then removed from the entire test surface of the plate by hand finishing with 600 grit paper and rubbing compound. The surface was cleaned with a weak phosphorous acid jelly after which a protective coat of wax was applied. Height-gauge measurements of the test surface indicated that local variations from flatness did not exceed 0.1 mm and were generally less than .03 mm.

A trailing-edge flap was added to the end of the flat plate in order to control the position of the attachment line on the leading edge. The flap balanced the wind-tunnel blockage between each side of

the plate in order to prevent leading-edge separation. The trailing-edge flap was adjustable from zero deflection to a maximum of 33 degrees toward the test side of the plate. The flap was constructed from a 1.83 m x 0.28 m x 0.02m fir board which was hinged at the plate-flap junction and had a tapered, sharp trailing edge.

### 2.3. Vibrating Ribbon

The source of the disturbances introduced into the boundary layer was a thin metallic strip which, when placed in a constant magnetic field, oscillated at the frequency of the electrical current passed through it. The ribbon material was a spring-tempered, phosphor-bronze alloy which was 0.025 mm thick and was obtained in precut widths of 2.5 mm.

Thirty electromagnets were mounted on the back of the plate in two parallel rows which resulted in the magnetic field visualized in Figure 2.7. The magnet configuration is shown in Figures 2.8. The two rows of magnets had opposite polarity to produce unidirectional field lines on the plate. The ribbon tension was applied using a spring scale which was accurate to within 1 Newton. A tension of 20 Newtons was found to be satisfactory. Ribbon clamps on the back of the plate held the ribbon in tension and provided electrical contact.

The freely vibrating length of the ribbon was generally 0.3 m and this length was centered at midspan of the plate. Each end of the vibrating length of the ribbon was held a distance of 0.1 mm from the plate by two layers of cellophane tape and the remaining stationary portion of the ribbon was isolated electrically from the plate by a

single layer of cellophane tape.

The variable parameters that affected the ribbon amplitude and frequency were the magnetic field strength, the alternating current in the ribbon, and the tension and length of the ribbon. Measurements of the ribbon amplitude and frequency as a function of the parameters mentioned above provided a direct indication of the disturbances introduced by the ribbon. These measurements were accomplished by means of the inductance probe which was mounted on the end of the traversing mechanism sting discussed in Section 2.5. A laboratory experiment was also set up to investigate the ribbon vibration characteristics in more detail.

A number of characteristics were important concerning the type of disturbances introduced by the ribbon. Measurements of the peak ribbon amplitude and spanwise phase were an indication of the uniformity of displacement. A spanwise plot of the ribbon phase relative to the driving signal, shown in Figure 2.9, indicated a first-mode ribbon vibration. The phase shift of 180 degrees was due to the polarity of the magnet connections. Spectrum analysis of the ribbon vibration also indicated that harmonics of the fundamental driving frequency were not present at the low ribbon amplitudes used in these experiments.

#### 2.4 Traversing Mechanism and Test Section Configuration

Two different traversing mechanisms were constructed to be used during different periods of the experiment. Most of the stability measurements were taken at the midspan of the plate and required only a

two-dimensional traversing mechanism for movement in the x- and y-directions shown in the test section layout of Figure 2.10.

The flat-plate model was mounted in a vertical plane, offset from the tunnel centerline. The x-traverse guide rods were mounted on the floor and ceiling of the tunnel and were parallel to the tunnel side walls. A typical flap deflection needed to balance the flow blockage is also shown in Figure 2.10.

The three-dimensional traversing mechanism shown in Figure 2.11 was used when spanwise measurements were required. The device was capable of moving 3.7 m in the x-direction, 1 m in the z-direction, and 100 mm in the y-direction. The x- and z-traverses were driven by stepping motors through a chain drive and had an accuracy of .25 mm. The y-traverse was also operated by a stepping motor, but it drove a precision lead screw and had an accuracy of .007 mm. All three traverses moved along precision-ground steel rods using self-aligning ball bushings. This support configuration provided low-friction linear motion and accurate positioning with a minimum of side-to-side motion.

The two-dimensional traversing mechanism shown in Figure 2.12 was capable of movement in the x- and y-directions. When spanwise measurements were not required, this device was used since it had less upstream influence on the mean-flow field than did the three-dimensional traverse. The two-dimensional traverse employed the same x and y drive mechanisms as did the three-dimensional traverse. However, elimination of the vertical guide rods, drive chain, and stepping motor permitted a reduction in the width of the main vertical support shroud from 100 mm to 13 mm. The influence of this traverse on the mean flow field is discussed in



### Chapter 3.

A more detailed discussion of the design criteria and specifications for the three-dimensional traverse is provided by Cousins, Saric, & Reynolds (1978). A complete report on the design and construction of the two- and three-dimensional traversing mechanisms can be found in Weber, Reynolds, & Saric (1979).

#### 2.5 Hot-Wire Sting

Placement of the hot-wire probe beyond the influence of the traversing mechanism was accomplished with the hot-wire extension arm or sting. The hot-wire sting was mounted on the y-traverse sliding block and extended 0.61 m to the side and 0.61 m ahead of the traversing mechanism as shown in Figures 2.11 and 2.12.

Because almost all hot-wire measurements were taken in the thin boundary-layer region near the plate, it was necessary to minimize the probe vibration. At the same time the sting thickness had to be kept small to reduce the upstream influence on the flow. These factors placed special requirements on the sting.

In order to obtain the needed rigidity and thin profile, a laminated composite construction was used. The sting was constructed at VPI & SU and consisted basically of two parts: the root and the extension. The root of the sting, which attached to the y-traversing mechanism, was a laminated Kevlar composite. This consisted of 20 layers of woven, pre-impregnated Kevlar material, which had an overall post-cure thickness of 4.76 mm after being subjected to a high temperature press. The extension arm which held the probe extension tube was a laminated

graphite composite, which was layed up from 21 layers of pre-impregnated, monodirectional graphite material. To obtain maximum strength in bending as well as torsion, the plies were layered with the following fillament orientation:  $0^\circ$ ,  $90^\circ$ ,  $+45^\circ$ ,  $-45^\circ$ ,  $90^\circ$ ,  $0^\circ$ . The resulting post-cure thickness of the graphite extension was 3.17 mm after being subjected to a high-temperature press. The two parts of the sting, the root and the extension, were butted end-to-end and laminated between two aluminum facing sheets, which resulted in a total thickness at the root of 6.35 mm. The hot-wire probe was mounted at the end of 4.76 mm o.d. stainless steel tube, which in turn was mounted at the end of the sting by a pen vise arrangement. This assembly is shown in Figure 2.13.

The sting configuration described above proved to be quite effective. The degree of vibration encountered was found to be well within tolerable limits and interference with the hot-wire measurements was not a problem.

To monitor the hot-wire probe position relative to the surface of the plate, an inductance probe was mounted at the end of the sting extension arm. By using this transducer, described in Section A.16 of the Appendix, the distance from the plate as well as the vibration relative to the plate was monitored.

#### 2.6. Fixed Probe Mount

Hot-wire measurements were also taken in the boundary layer using the fixed probe mount shown in Figure 2.14. This probe mount was taped directly to the surface of the plate and was used primarily as a diagnostic tool to allow comparison with signals obtained from a hot-wire probe

mounted on the traverse sting. The fixed probe mount was also used to determine the transition Reynolds number on the flat plate model. Specific applications for this mount are described in Chapter 3.

## CHAPTER 3

### EXPERIMENTAL PROCEDURES AND RESULTS

#### 3.1 Basic Measuring Devices and Instrumentation

The primary objective of these experiments was to investigate the character and linear stability of small disturbances introduced into the laminar boundary layer. As described in Chapter 2, disturbances were introduced into the boundary layer by a vibrating ribbon. Various properties of these disturbances were then measured by hot-wire anemometry.

Three independent constant temperature anemometer channels were used to measure the disturbance velocities and mean flow velocity. Each channel consisted of a DISA 55D01 Constant Temperature Anemometer (CTA), a DISA 55D10 Linearizer, and a DISA 55D35 RMS Unit. These units are described in section A.1 of the Appendix. Probe calibration was accomplished by comparison with a Dwyer 160-DCF pitot static tube located 300 mm ahead of the leading-edge of the model. A simple arrangement used for the signal conditioning of a constant-temperature anemometer output is shown in Figure 3.1. All of the anemometer outputs were linearized to provide an output voltage proportional to the velocity being measured. Hot-wire probes were not temperature compensated, but instead were occasionally relinearized to account for daily temperature variations. Linearization of hot-wire probes was handled through the HP 3052A Automatic Data Acquisition System, as was much of the data gathering process. The data acquisition system consisted of a HP3495A and HP3455A

scanning voltmeter which sampled the data, and then sent the digitized information to a HP9825A calculator/printer and to a HP 9872A plotter. These units are described in Section A.2 of the Appendix.

The hot-wire probes used were generally of the boundary-layer type, allowing measurements to be taken close to the surface of the model. A 3 mm long, 5  $\mu$ m diameter platinum-plated tungsten wire with gold plated ends served as the measuring device. The sensing portion of the wire was 1.25 mm long ( $L/D = 250$ ) and was isolated from the support prongs by the unheated portion of wire at the ends. The probe body and sensor configuration are described in Section A.2 and shown in Figures A.1-A.3 of the Appendix.

### 3.2 Mean Flow Measurements

A number of preliminary measurements were necessary in order to assure that the flow past the model was two-dimensional. The velocity of the mean flow was found to be uniform across the test section until the side wall boundary layer was encountered. Moreover, the freestream velocity was found to be steady over the working range of wind tunnel speeds.

The development of a Blasius boundary layer takes place under the conditions of zero streamwise pressure gradient. Due to the physical limitations of the wind tunnel facility, zero pressure gradient flow was not entirely possible. The test section used for these experiments did not have adjustable walls and had a constant cross-sectional area. As a result, blockage effects due the wall boundary layers, the traversing mechanism, and the model itself were accounted for by correct position-

ing of the model. The overall effect of these factors on the chordwise and spanwise pressure gradient was measured on the plate by the series of static pressure ports shown in Figure 2.6. The 93 pressure ports were connected to two, 48 port Scanivalves (Section A.17) which relayed the pressure signal to a differential pressure transducer with a full-scale range of  $\pm 0.5$  mm Hg. The pressure transducer used was a Setra Systems Model 239E and is described in Section A.15 of the Appendix. Blockage effects due to the traversing mechanism were minimized by positioning the plate closest to the back wall of the test section. The plate was also placed at a slight positive angle of attack to compensate for boundary-layer growth on the test side of the plate. A balance in the blockage between the front and back side of the plate was achieved by using the trailing-edge flap. By deflecting the flap toward the test side of the plate, the leading-edge stagnation point could be positioned at the tip of the leading edge. As a precaution, the stagnation point was positioned slightly back from the leading edge toward the test side of the plate. In this way, the possibility of leading edge separation due to a slight imbalance in the blockage was avoided. This configuration of the flat-plate model, traversing mechanism, and trailing edge flap is shown in Figure 2.10. Chordwise and spanwise pressure gradients taken with this test configuration are plotted in Figures 3.2 and 3.3. A pressure rise at the trailing edge was the result of deceleration of the flow just prior to the trailing-edge flap. A zero spanwise pressure gradient existed to within  $C_p = \pm 0.1\%$  over an 0.8 m wide region along the centerline of the plate. Figures 3.2 and 3.3 indicate that the probe mounted on the traverse sting was outside the region of decreasing

pressure created ahead of the traversing mechanism. In order to substantiate this further, measurements were made to determine the effect of the traversing mechanism on the behavior of the disturbances themselves. This was accomplished by rigidly mounting a hot-wire probe support to the flat plate so that disturbance amplitudes could be measured for different traverse positions.

A mounting bracket shown in Figure 2.14 was taped to the plate and this was used to hold a DISA 55A22 hot-wire and probe support in the boundary layer of the flat plate. The fixed hot-wire was displaced about 25 mm from the centerline of the plate so that the probe support tube mounted on the traverse sting could move alongside it. Disturbances at a dimensionless frequency of  $F = 55 \times 10^{-6}$  were introduced into the boundary layer by the vibrating ribbon. The T-S waves were in the region of amplification at the location of the fixed probe. The disturbance amplitude was measured by the fixed probe with the sting mounted probe alongside it, thereby simulating a measurement taken by the sting mounted probe. Measurements were also taken with the traverse moved aft to remove any influence it may have had on the fixed probe readings. After a careful streamlining of the traversing mechanism, this procedure showed that the traversing mechanism had no measurable influence on the disturbances encountered by a hot-wire probe mounted on the traverse sting.

As a final verification of zero pressure gradient flow, the growth of the boundary layer on the flat plate was compared with that predicted for a Blasius boundary layer. If the boundary layer is truly a Blasius

boundary layer, measurements of displacement thickness,  $\delta^*$ , at arbitrary  $x$  locations will provide a virtual position of the leading edge which does not change relative to the actual leading edge. This was in fact the case and the virtual leading edge was found to be at  $x \approx + 89$  mm.

Laminar boundary-layer profiles taken on the plate also compared well with those predicted for a Blasius boundary layer. This comparison is made in Figure 3.4.

The free-stream turbulence level of the flow plays a major role in controlling the location of transition from a laminar to a turbulent boundary layer. The  $u$ -component of the turbulence level in the free-stream was measured using the single-wire boundary-layer probe (see Section A.2.1) as well as a parallel array two-wire turbulence probe (see Section A.2.2). The parallel wire configuration provided a means for the elimination of electronic noise by removing the uncorrelated portion of the signal. However, spectrum analyses of the anemometer output, shown in Figure 3.5, indicated that the frequency range of the naturally occurring turbulence is much lower than the high frequency electronic noise. Therefore the values of  $|u|$  given in Table 3-1 were obtained by the single-wire boundary-layer probe with the electronic noise above 1 kHz filtered by a Tektronix AM 502 Differential Amplifier. No variations in the free-stream turbulence were found over the uniform flow region of the test section.

The influence of freestream turbulence on the location of transition was first investigated in detail by Schubauer and Skramstad (1947). These investigations showed that as the freestream turbulence was decreased the transition Reynolds number,  $R_T$ , increased. However, a



maximum in  $R_T$  was found (i.e.  $(R_T)_{\max} = 2.8 \times 10^6$ ) for very low free-stream turbulence levels. Later experiments by Wells (1967) and Spangler & Wells (1968) suggested a dependence, not only on the magnitude of the turbulence, but on the spectral content as well.

During early phases of the experiment, the traversing mechanism described in Chapter 2 was not yet in operation. Transition measurements were then made using a hot-wire probe rigidly mounted on the surface of the flat plate, as discussed earlier. As the free-stream velocity was increased, the onset of transition was displayed as a sharp increase in the boundary-layer velocity. Because of the transient nature of the transition process, numerous samples of the hot-wire reading were taken and averaged by the data acquisition system. This procedure resulted in the data given in Figure 3.6. The beginning of the transition process from a laminar to a turbulent boundary layer occurred at  $R_T \approx 3.5 \times 10^6$ . In general, transition due to natural growth of laminar boundary-layer disturbances occurred at  $R_T = 3.3 \times 10^6$  to  $3.6 \times 10^6$ . These high values of  $R_T$  were comparable to values obtained at the excellent facilities at the U. S. National Bureau of Standards and the Institute of Theoretical and Applied Mechanics (U.S.S.R).

### 3.3 Boundary-Layer Stability Measurements

The spatial growth and decay of disturbances were measured in the boundary layer using a hot-wire anemometer. Disturbances were artificially introduced into the boundary layer by the vibrating metallic ribbon which was discussed in Chapter 2.

The theory of Tollmien (1929) and Schlichting (1933) and experimental verification by Schubauer and Skramstad (1947), Ross et al (1970) Kachanov et al (1975), and Strazisar et al (1975) have established that growth or decay of disturbances depends not only on spatial locations, i.e., the Reynolds number, but also on frequency. At a given Reynolds number there is a discrete frequency band of disturbances which are amplified while all others are damped. Likewise, for a given frequency, there is a region from  $R_I$  to  $R_{II}$  which has amplified waves while outside this region the waves decay. This is the behavior predicted by the neutral stability curve shown in Figure 1.3. Therefore, locations of neutral stability can be determined either by keeping the frequency constant and varying  $x$  or vice versa. In the experiments described in this report, locations of neutral stability, or zero growth rate, for a certain frequency of disturbance are found by moving a hot-wire probe in the  $x$ -direction until a maximum or minimum in the disturbance amplitude is found.

Because the disturbance amplitude is not constant across the boundary layer, but has some characteristic profile which is a function of  $y$  as well as  $x$ , there is some ambiguity as to where in the boundary layer the disturbance amplitude should be measured. A typical disturbance profile obtained experimentally is plotted in Figure 3.7 against that predicted by the parallel stability theory. Various experimental methods have been used to measure the growth or decay in the disturbances as they propagate in the streamwise direction. The most commonly used methods have been to measure the disturbances at various streamwise

locations keeping  $y$  constant (Schubauer and Skramstad 1947). One of the methods used by Ross et al (1970) was to keep the boundary-layer similarity variable,  $\eta = y(U_\infty/\nu x)^{1/2}$ , at a constant value. Measurements of the disturbance profile at various streamwise locations have shown that the disturbance profile shifts or distorts along lines of constant  $y$  or constant  $\eta$ . The nonparallel theory of Saric and Nayfeh (1977) showed that errors due to profile distortion were minimized by following the maximum of  $|u|$  as the streamwise location was varied. This method was used by Kachanov et al (1975) and Strazisar et al (1975) and was used here to determine the growth and decay of boundary-layer disturbances. These measurements of Tollmien-Schlichting waves at the maximum of  $|u|$  are described in the remainder of this section.

Disturbances were introduced into the boundary layer at a given frequency supplied by a Spectral Dynamics SD104A-2 Sweep Oscillator (Section A.7). The oscillator signal was amplified by a McIntosh Model 100 Power Amplifier (Section A.8) which was adjusted to produce the desired disturbance amplitude. Linear stability measurements were performed with  $u_m$  less than 0.1% of the free-stream velocity,  $U_\infty$ . At this low level, boundary-layer disturbances introduced by the vibrating ribbon were only a part of the total signal picked up by the hot-wire probe.

Components of the hot-wire signal other than the component at the ribbon frequency were due to high frequency electronic noise, probe vibration and naturally introduced disturbances from the free stream. Signal processing of the anemometer output was accomplished according

to the instrumentation flow chart in Figure 3-8. A detailed description of this instrumentation is given in the Appendix.

A Tektronix AM 502 Differential Amplifier, was used to remove the high frequency electronic noise from the linearized anemometer signal and the remaining signal from 0.1 Hz to 300 Hz was amplified. In the resulting signal, the naturally occurring disturbances were very small but the component due to vibration appeared quite large.

The vibration of the traverse and probe sting was monitored by a Bently Nevada inductance-type proximity probe (Section A.16) located on the end of the sting. The sting and proximity probe are shown in Figure 2.13. The frequency spectra of the anemometer and proximity probe outputs were obtained using a HP 5420A Digital Signal Analyzer (Section A.4) or a Zonics Multichannel FFT Processor (Section A.5). Vibration of the hot-wire probe in the boundary-layer introduced a fluctuating mean velocity at the probe sensor and this was observed on the anemometer output. A typical frequency spectrum of the anemometer output for a hot-wire probe located in the linear region of the boundary-layer velocity profile is shown in Figure 3.9. A corresponding spectrum of the proximity probe output is shown in Figure 3.10. The spectrum shown in Figure 3.10 reveals the frequency content of the sting vibration. Comparison of Figures 3.9 and 3.10 show that frequency components exist in the anemometer output which correspond to some of the frequency components from the proximator. Inspection of these specific disturbance frequencies revealed that they were not T-S waves. Confirmation that these components common to both the anemometer and the proximator outputs were in fact vibration was provided by measurements using the

fixed probe mount discussed earlier. The fixed probe measurements showed that the only components present in the boundary-layer flow were the very low level background T-S waves and the T-S wave introduced by the vibrating ribbon. The actual magnitude of the probe vibration was determined by reading the peak a.c. voltage from the proximator output. This was accomplished using a Bruel & Kjaer 2427 Autoranging Digital Voltmeter (Section A.14). Using the inductance probe, the amplitude of the sting vibration was found to be  $y \approx .05$  mm at a free stream velocity of 15 m/s. These measurements indicate that the probe vibration was very small, generally less than 1% of the boundary-layer thickness. Vibration of this size had a negligible effect on measurements of the disturbance amplitudes.

A narrow band-pass tracking filter facilitated measurement of only the disturbances introduced at the ribbon frequency. A Spectral Dynamics SD 121 Tracking Filter (Section A.10) served this purpose. The tracking filter with a 1 Hz band width was tuned to the ribbon frequency by using the sweep oscillator. The filter could also be switched out to pass the entire unfiltered disturbance signal. A measure of the r.m.s. disturbance amplitude was obtained using a DISA 55D35 RMS Unit (Section A.1) and a qualitative evaluation was gained by monitoring the signal on a Tektronix 5113 oscilloscope. By using the oscilloscope, the filtered or unfiltered disturbance signal was compared with the ribbon input from the oscillator and the traverse vibration from the proximator. This was a valuable diagnostic tool for monitoring the different parameters influencing the measurements. A quantitative measure of the system was then obtained by using the spectrum analyzer and data acquisition system.

With the tracking filter in the filter mode, the maximum of the r.m.s. disturbance amplitude was found by varying the y-probe coordinate. This process was aided by plotting  $|u|$  vs.  $y$  on an analog plotter. Several passes of the probe around the location  $\eta = \eta_c$  revealed the peak in the disturbance profile. The probe was then moved back to the location of  $u_m$  and this value, along with the corresponding x-probe location, was sampled by the data acquisition system. This procedure was repeated at successive chordwise probe locations and the results were plotted on a HP 9872A Digital Plotter (Section A.2). The x and y coordinates were obtained from the traversing mechanism controller unit (Section A.11). The process of following a trajectory of  $|u| = u_m$  was continued until a neutral point was found, i.e.  $(du_m/dx) = 0$ . For decaying waves this corresponded to a minimum or branch I point, and for amplified waves a maximum was found corresponding to a branch II point. In this way, the neutral stability points in Figure 3.11 were determined. The Reynolds number at the neutral point was determined based on integration of the mean boundary-layer velocity profile and the assumption of a Blasius boundary layer.

Determination of the neutral stability points based on measurements at  $u_m$  show very good agreement with the theory as well as with the experimental data of previous investigators shown in Figure 1.3. The data shown in Figure 1.3 was measured using various methods. The data of Schubauer and Skramstad (1947) was taken by following trajectories of constant  $y$  while that of Ross et al (1970) was taken using a combination of the methods discussed earlier. Data obtained by Strazisar et al

(1975) and Kachanov et al (1975) was taken by following  $|u|_{\max}$ . Variations in experimental data at the high frequencies are due to the various methods used as well as to the difficulty of the measurements at the higher frequencies.

TABLE 3.1. FREE STREAM TURBULENCE LEVELS

m/s	%
$U_{\infty}$	$ u /U_{\infty}$
9	.018
12	.018
15	.022
20	.028
30	.045



## CHAPTER 4

### CONCLUDING REMARKS

Experiments to investigate laminar boundary-layer stability and the effects of laminar flow control have been developed at VPI & SU. This program was initiated with the investigation of the linear stability of the Blasius boundary layer. These experiments on a flat-plate model have served to develop the experimental apparatus and measurement techniques for future studies involving laminar flow control and flow past three-dimensional models. Comparisons of the results with existing neutral stability results have served to verify the experimental methods to be used in the later studies.

The experiments were performed in the VPI & SU Stability Wind Tunnel, which is normally used for aerodynamic loading and stability experiments. It was therefore necessary to establish the feasibility of conducting boundary-layer stability experiments in this facility. This investigation showed that the facility is very suitable for boundary-layer stability measurements. The freestream turbulence levels were found to be very low and were comparable with other facilities used for this type of work. Measurements to determine the flow uniformity and steadiness revealed no unusual or undesirable features in the flow. Confirmation of the wind-tunnel flow quality was provided by a determination of the transition Reynolds number. Future measurements of the transition Reynolds number using a total pressure tube will provide a more complete comparison with other facilities.

Due to the test section configuration, the flow exhibited a negative pressure gradient in the streamwise direction. However, a zero chordwise pressure gradient was accomplished on the model by placement of the plate at a slight positive angle-of-attack. The use of a trailing-edge flap then balanced the flow blockage and aligned the flow with the flat-plate model. With this test configuration the boundary layer was found to be laminar and measurements of the velocity profiles indicated that it was similar with respect to the boundary-layer variable  $\eta = y(U_\infty/\nu x)^{1/2}$ . Measurements of the boundary-layer displacement thickness also agreed well with that predicted for a Blasius layer, within a small correction for pressure gradient effects at the leading edge. This correction due to the leading-edge pressure gradient was a constant for a given free-stream velocity. At a given velocity a virtual leading edge was determined from the measurement of displacement thickness. Reynolds number calculations at that velocity were then based on the distance from this virtual leading edge.

Tollmien-Schlichting waves were generated in the boundary layer by using a vibrating ribbon and the linear stability of these waves was investigated. Neutral stability points were found for several disturbance frequencies which are shown in Figure 3.11. These measurements were taken by following the maximum of  $|u|$  and the Reynolds number is based on the reference length  $\delta_r = (\nu x/U_\infty)^{1/2}$ . Additional experiments on neutrally stable as well as amplified waves are needed to fully verify the experimental procedures used thus far. However, the neutral stability points shown thus far have exhibited good agreement with previous experimental results obtained in other facilities.

With the existing experimental facility a number of other experiments are now possible. Preliminary measurements have been made investigating the behavior of two Tollmien-Schlichting (T-S) waves in a Blasius boundary layer when the waves display weakly nonlinear behavior. This behavior was measured for large amplitude, single frequency disturbances ( $|u|/U_\infty = 0.6\%$ ) introduced by the ribbon. Two frequency disturbances were also introduced using a single ribbon and a specially designed signal mixer. The initial amplitudes of the two disturbances were carefully controlled and their subsequent growth and interaction were monitored using a spectrum analyzer. Measurements were also taken of the ribbon vibration characteristics to determine the response of the ribbon at large amplitudes. The experiments were motivated by the need for information leading to an understanding of the evolution of nonlinearly interacting T-S waves before the occurrence of transition.

Experiments are also being conducted to examine nonparallel effects on boundary-layer disturbances due to the growth of the boundary layer. The effects of laminar flow control will also be considered with the addition of suction panels to the flat plate model. Experiments on three dimensional swept wing models will follow the flat plate experiments. The three dimensional traversing mechanism will be employed in these experiments for measurement of spanwise disturbance propagation.

# REFERENCES

- Bradshaw, P. 1965 The effect of wind tunnel screens on nominally two-dimensional boundary layers. J. Fluid Mech. 22 679.
- Bouthier, M. 1973 Stabilité linéaire des écoulements presque parallèles, II - La couche limite de Blasius. J. de Mécanique 12, 75.
- Cousins, W. T., Saric, W. S., & Reynolds, G. A. 1978 Design of a three dimensional traverse mechanism for boundary layer stability studies. VPI & SU Rep. No. VPI-E-78-13.
- Gaster, M. 1974 On the effects of boundary-layer growth on flow stability. J. Fluid Mech. 66, 465.
- Kachanov, Yu. S., Kozlov, V. V. & Levchenko, V. Ya. 1975 Growth of small disturbances in a laminar boundary layer. (in Russian) Ucheniye Zapiski TSAGI 5, 137.
- Kachanov, Yu. S., Kozlov, V. V., & Levchenko, V. Ya. 1977 Nonlinear development of waves in a boundary layer (in Russian) Mek. Zhid. i Gaza No. 3, 49.
- Kachanov, Yu. S., Kozlov, V. V., & Levchenko, V. Ya. 1978 Experiments on nonlinear interaction of waves in a boundary layer. AIAA Paper No. 78-1131.
- Nayfeh, A. H. & Bozattli, A. N. 1978 Nonlinear interaction of waves in boundary layer flows. VPI & SU Rep. No. VPI-E-79.6.
- Nayfeh, A. H., Saric, W. S. & Mook, D. T. 1974 Stability of nonparallel flows. Arch. Mech. Stosow 26, 401.
- Ross, J. A., Barns, F. H., Burns, J. G., & Ross, M. A. S. 1970 The flat plate boundary layer, Part 3, Comparison of theory with experiment. J. Fluid Mech. 43, 819.
- Saric, W. S. & Nayfeh, A. H. 1975 Nonparallel stability of boundary layer flows. Phys. Fluids 18, 945.
- Saric, W. S. & Nayfeh, A. H. 1977. Nonparallel stability of boundary layers with pressure gradients and suction. AGARD Paper No. 6, Proceeding No. 224.
- Schlichting, H. 1933 Zur Entstehung der Turbulenz bei der Plattenströmung. Nachr. Wiss. Göttingen Math.-phys. Klasse, p. 181-208.
- Schubauer, G. B. & Skramstad, H. K. 1947 Laminar boundary layer oscillations and transition on a flat plate. J. Res. Nat. Bur. Stand. 38, 251.

- Spangler, J. G. & Wells, C. S. Jr. 1968 Effects of freestream disturbances on boundary-layer transition. AIAA J. 6, 543.
- Strazisar, A. J., Prahl, J. M., & Reshotko, E. 1975 Experimental study of the stability of heated laminar boundary layers in water. Case Western Reserve Univ. Dept. Fluid Thermal Aerosp. Sci. FTAS/TR-75-113.
- Tollmien, W. 1929 Über die Entstehung der Turbulenz. Nachr. Ges. Wiss. Gottingen, Math.-phys. Klasse, pp. 21-44.
- Weber, D. L., Reynolds, G. A., & Saric, W. S. 1979 Design and construction of a three-dimensional and two-dimensional traversing mechanism with a digital controller. VPI Report (in preparation).
- Wells, C. S. Jr. 1967 Effects of freestream turbulence on boundary layer transition. AIAA J. 5, 172.

## APPENDIX

A.1. DISA ANEMOMETRY. Three independent anemometry channels were used. Each channel consisted of:

A.1.1. DISA 55D01 Constant Temperature Anemometer (CTA). The anemometer was operated with a bridge ratio of 1:20, using a probe cable length of 5m. For high resolution measurement of low-level signals the hot wires and cables were balanced at a gain of 11 and operated at a gain of 7. The anemometer output voltage  $V$  was related to the air velocity  $U$  by:  $V^2 = V_0^2 + BU^n$ , where  $V_0^2$ ,  $B$ , and  $n$  are functions of temperature.

A.1.2. DISA 55D10 Linearizer. All anemometer outputs were processed through this unit to obtain a voltage signal which was linearly proportional to the velocity being measured. The unit was calibrated by inputting  $1/n$ , obtained by a plot of  $\log U$  vs.  $\log[(V/V_0)^2 - 1]$  from the anemometer. This procedure was handled through the data acquisition system.

A.1.3. DISA 55D35 RMS Voltmeter. A true r.m.s. and squared r.m.s. was obtained in the range - 60 dB to + 50dB over one volt. The integrator time constant was variable in the range 0.3 to 100 seconds.

A.2. DISA HOT-WIRE PROBES

A.2.1. DISA 55P05 Boundary-Layer Probe. The sensor consisted of a 5  $\mu$ m diameter Platinum-plated tungsten wire with an overall length of 3 mm and a sensitive wire length of 1.25 mm ( $L/D = 250$ ). Sensor-support prong isolation was provided by a copper and gold plating at the wire ends to a diameter of approximately 30  $\mu$ m. This configuration is shown in Figure A.1.

A.2.2. DISA 55P71 Parallel-Array Turbulence Probe. This was a two wire probe with parallel sensors as shown in Figure A.2. The probe sensors measured essentially at the same point and this allowed elimination of electronic noise from the two independent channels.

A.2.3. DISA 55A22 General Purpose Hot-Wire Probe. This is the old style DISA probe and was used for fixed probe applications as mentioned in Section 3.2. This probe configuration is shown in Figure A.3.

- A.3. HP 3052 AUTOMATIC DATA ACQUISITION SYSTEM. This system provided high speed, 40 channel, data sampling capabilities. In addition, data processing capabilities were provided by the calculator with output via paper tape or digital plotting. The system consisted of:
  - A.3.1. HP3455A High Accuracy/High Resolution DVM.
  - A.3.2. HP 3495A Input Multiplexer.
  - A.3.3. HP 9825A High Performance Calculator and ROMS.
  - A.3.4. HP 9872A Four-Pen Digital Plotter.
- A.4. HP 5420A DIGITAL SIGNAL ANALYZER. This is a two channel digital instrument which provides time and frequency domain analysis of analog signals in the range of dc to 25 kHz. Analog data is input through the HP 54410A Analog/Digital Converter and anti-aliasing is provided by a HP 54470 Digital Filter.
- A.5. ZONIC MULTICHANNEL FFT PROCESSOR. A two channel spectrum analyzer, the Zonic provided high frequency analyzing capabilities up to 50 kHz.
- A.6. HP 3960 INSTRUMENTATION TAPE RECORDER. This unit was a portable, 4 channel, 3-speed tape recorder which uses 6.35 mm magnetic tape. The recorder could be operated in either FM mode or direct record mode. It was used in FM mode which provided a dc to 5 kHz frequency bandwidth.
- A.7. SPECTRAL DYNAMICS SD104A-2 SWEEP OSCILLATOR. A constant 1v amplitude wave from 0.02 Hz to 20 kHz,  $\pm 0.2$  dB was provided by this instrument. It was operated in the manual, constant frequency mode for these experiments but had linear and logarithmic frequency sweeping capabilities.
- A.8. MC INTOSH MODEL 100 AC POWER AMPLIFIER. This unit provided a 100 watt output at 8 ohms to the vibrating ribbon. The frequency response was 10 Hz to 50 kHz, -0.5 dB at 100 watts.
- A.9. SORENSEN-NOBATRON DCR150-15A. This was a dc power supply used to drive the electromagnets. It had a 15 amp maximum output.
- A.10. SPECTRAL DYNAMICS SD121 TRACKING FILTER. This unit was a narrow-band pass filter which was tuned to a reference signal input. It was used with a bandwidth of 1 Hz, and bandwidths of 2, 10, 50, 100, 200 were also available.

- A.11. TRAVERSE CONTROLLER. Pulses to all three traversing mechanism stepping motors were provided by Superior Electric ST103 Translator. This unit was supplemented by a controller/counter which provided convenient selection of motor stepping modes available through the ST103. These include half step/full step, low speed/high speed, and continuous run/single step options. Motor steps were also counted by the Traverse Controller and were output in a binary led display as well as front panel mounted DVM and corresponding analog voltage output.
- A.12. TEKTRONIX MODEL 5113 OSCILLOSCOPE. This is a 8-channel scope with 2-channel storage capabilities.
- A.13. HP 5300A/5302A FREQUENCY COUNTER. This counter provided frequency measurements with a resolution of 0.1 Hz for a ten second sample period.
- A.14. BRUEL & KJAER 2427 AUTORANGING DIGITAL VOLTMETER. This voltmeter provided a true r.m.s., average, or peak reading for input signals in the range 0.5 Hz to 500 kHz.
- A.15. SETRA SYSTEMS MODEL 239E DIFFERENTIAL PRESSURE TRANSDUCER. This was a  $\pm 0.01$  psid transducer which provided a linear dc output of  $\pm 2.5$  volts.
- A.16. BENTLY NEVADA SERIES 190 PROXIMITOR PROBE/SERIES 3000 SIGNAL CONDITIONER. This is an inductance type probe which has a linear measuring range of 0 - 1.1 mm with a nominal output of 0.0 to - 14 vdc. The frequency response was d.c. to 10 kHz,  $\pm 1\%$ .
- A.17. SCANIVALVE MODEL D. This solenoid operated mechanism provided for serial sampling of 48 pressure inputs. The selected pressure input was then available for pressure transducer measurement.



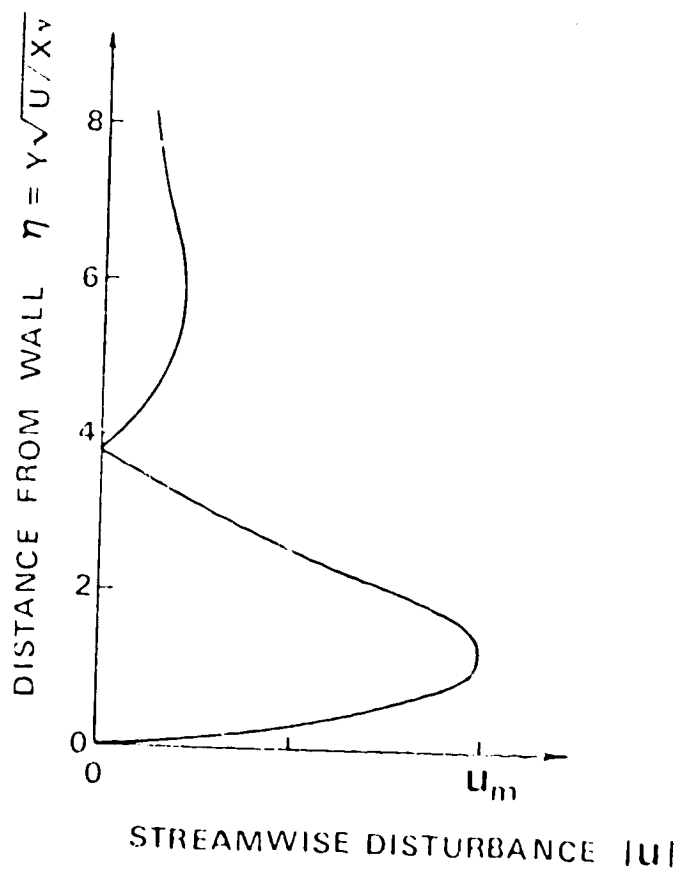


Figure 1.1 Example of streamwise disturbance velocity for the case of  $F = 86 \times 10^{-6}$ ,  $R = 440$ .

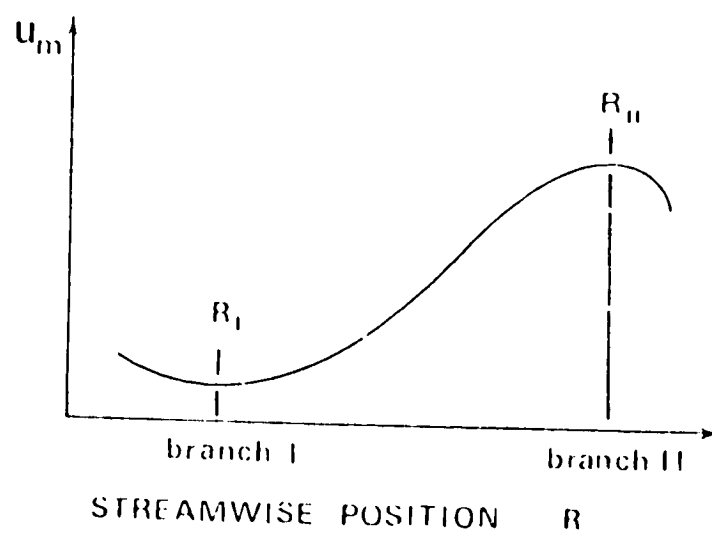


Figure 1.2 Schematic of amplitude growth and neutral stability point determination.

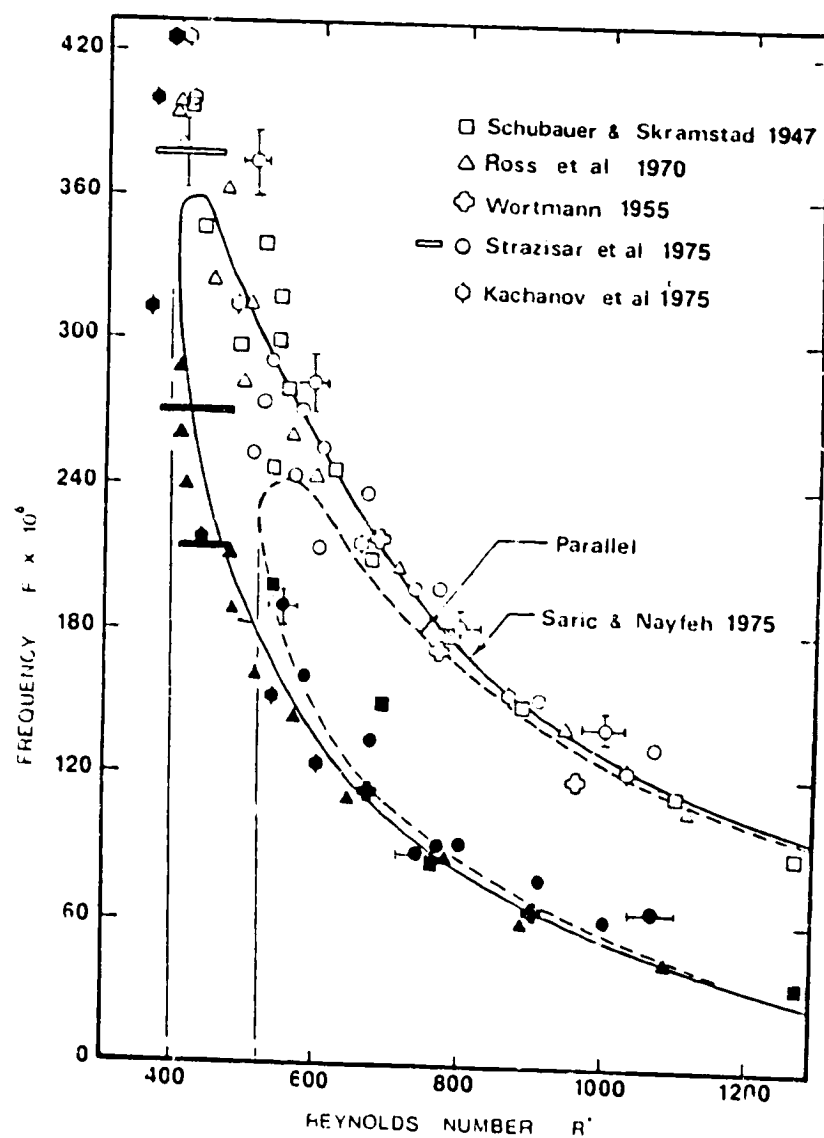
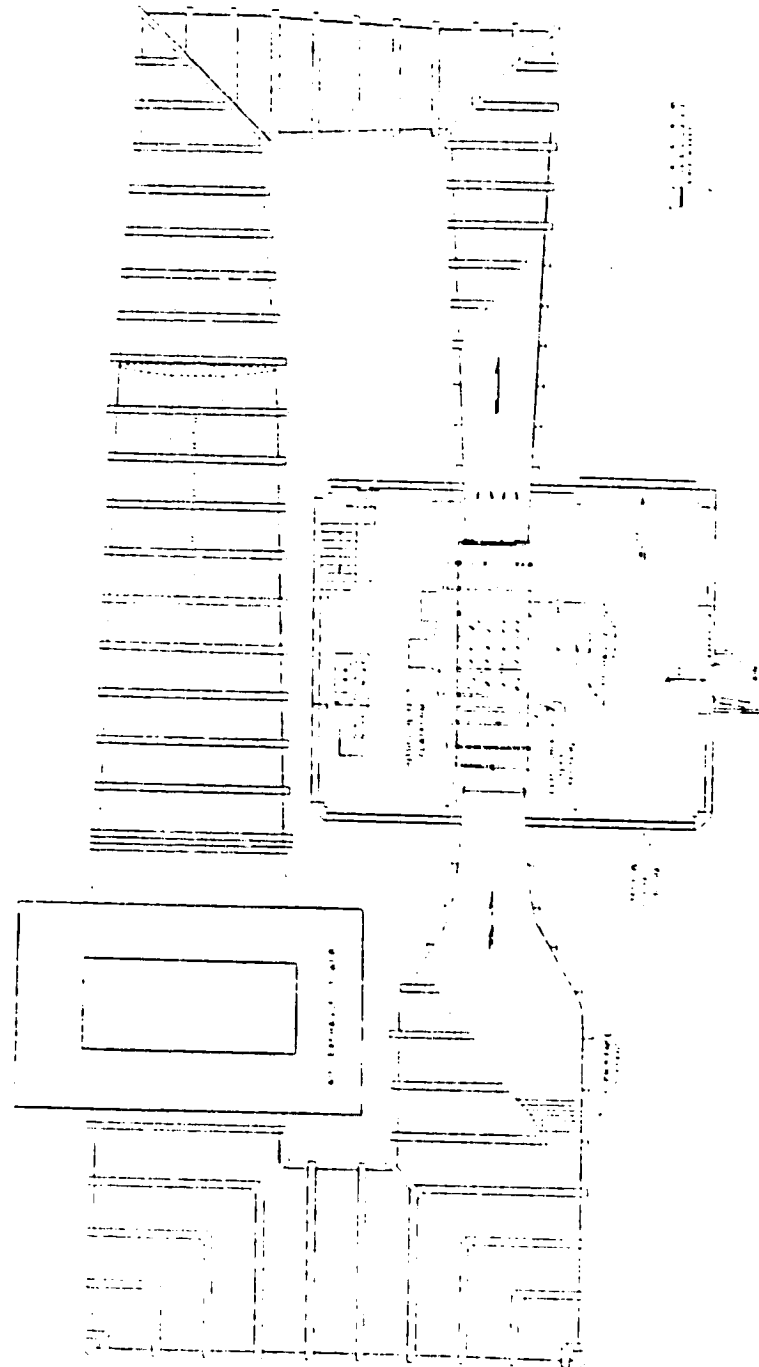


Figure 1.3 Neutral stability curve for Blasius boundary layer. Solid symbols are branch I experimental points. Open symbols are branch II. The critical displacement thickness Reynolds number is 400 for nonparallel calculations, 520 for parallel calculations.



ORIGINAL PAGE IS  
OF POOR QUALITY

Figure 2.1 VPI & SU Stability Wind Tunnel.

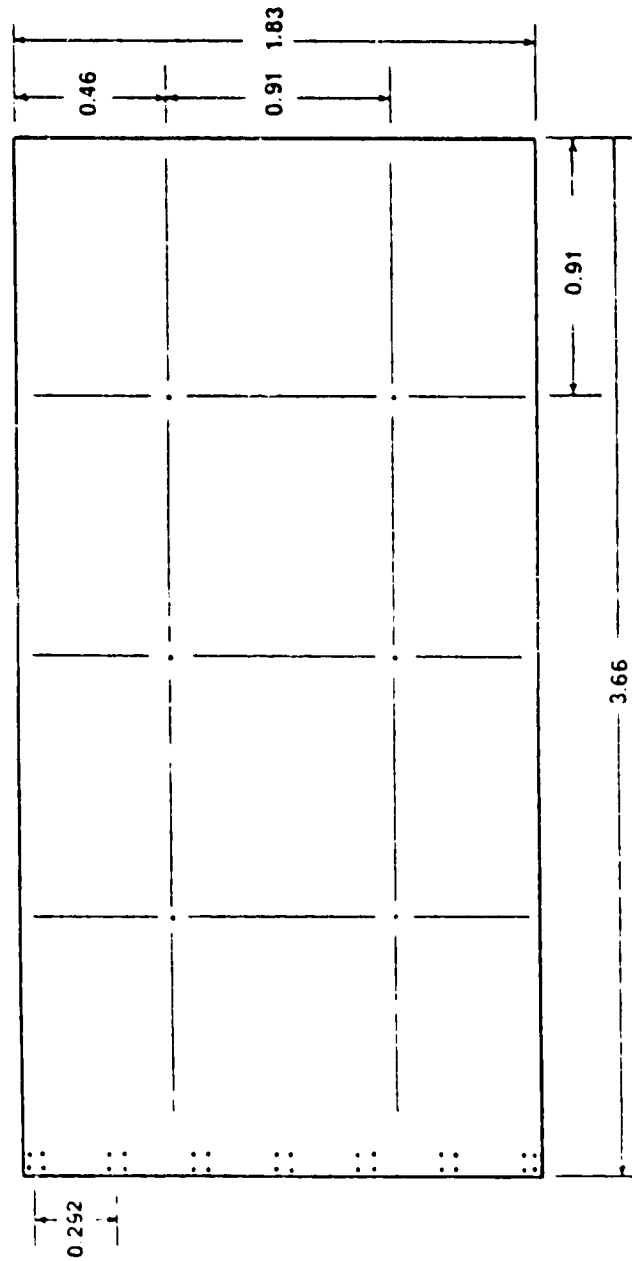


Figure 2.2 Locations of the 34,  $\frac{1}{4}$  x 28 threaded inserts on the back of the flat plate model. All dimensions in meters.

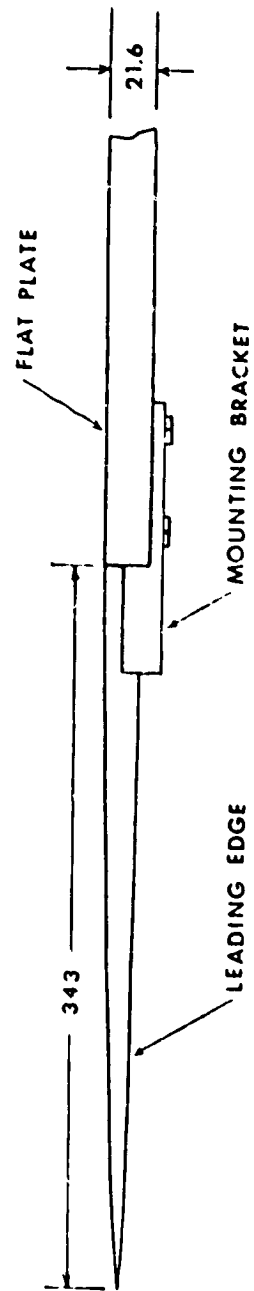


Figure 2.3 Leading edge-flat plate junction. All dimensions in millimeters.

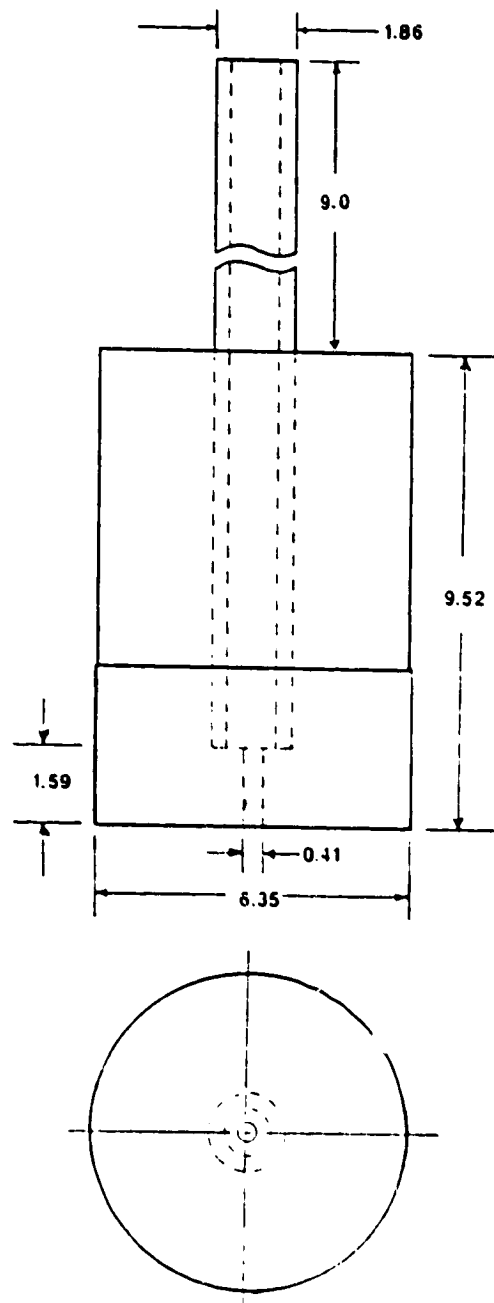


Figure 2.4 Static pressure port insert. All dimension in millimeters.

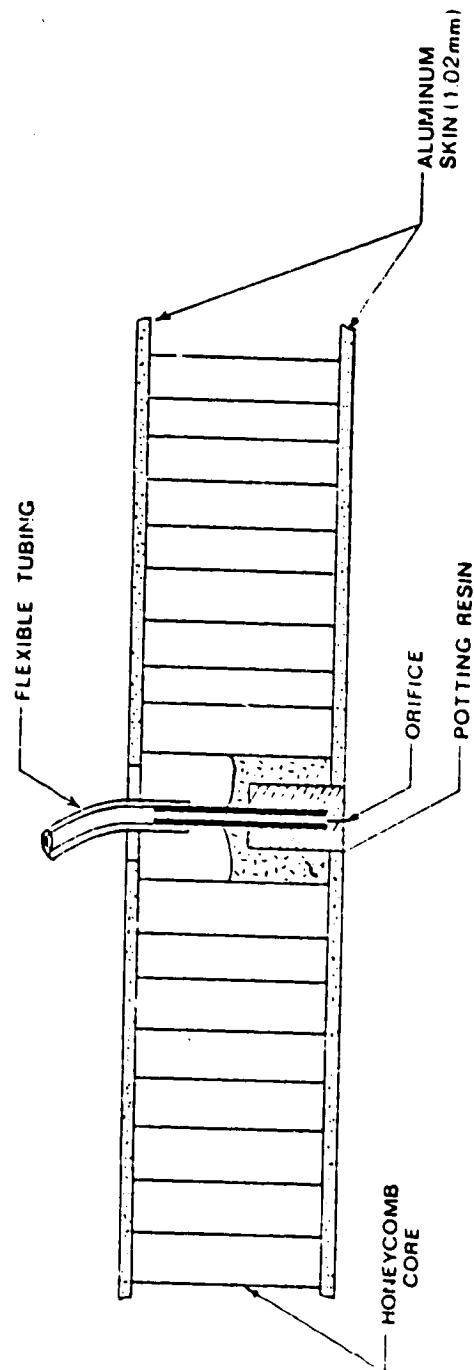


Figure 2.5 Static pressure port assembly and plate cross-section.



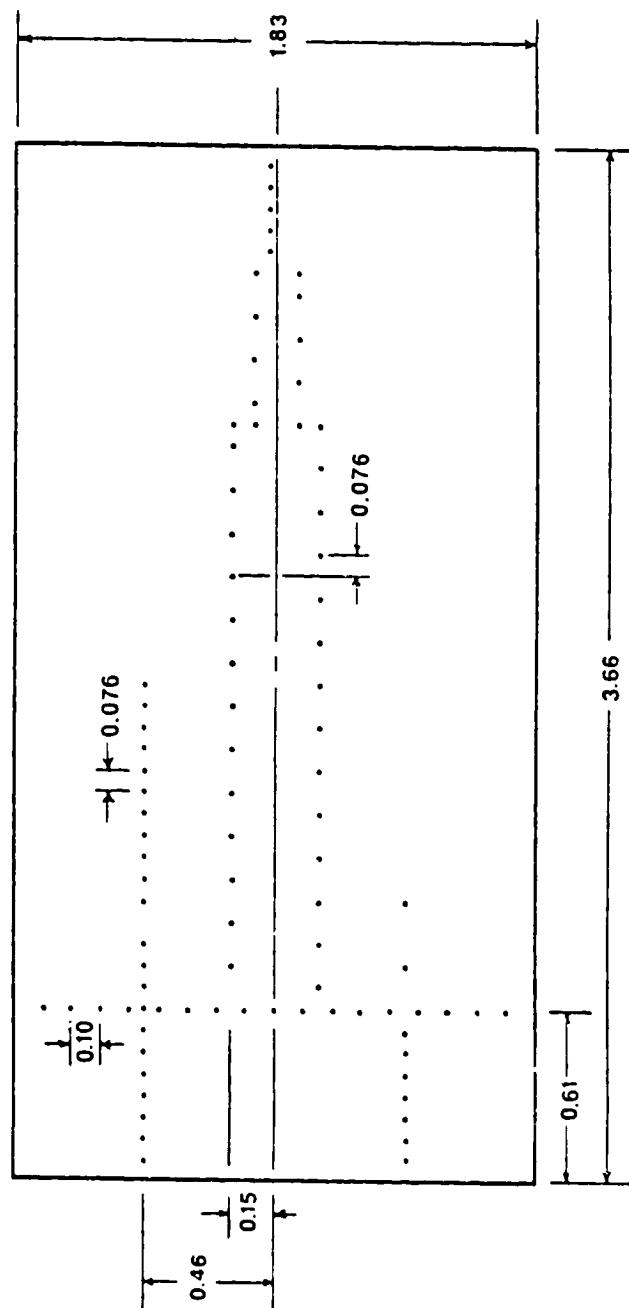


Figure 2.6 Static pressure port distribution on flat plate model. All dimensions in meters.

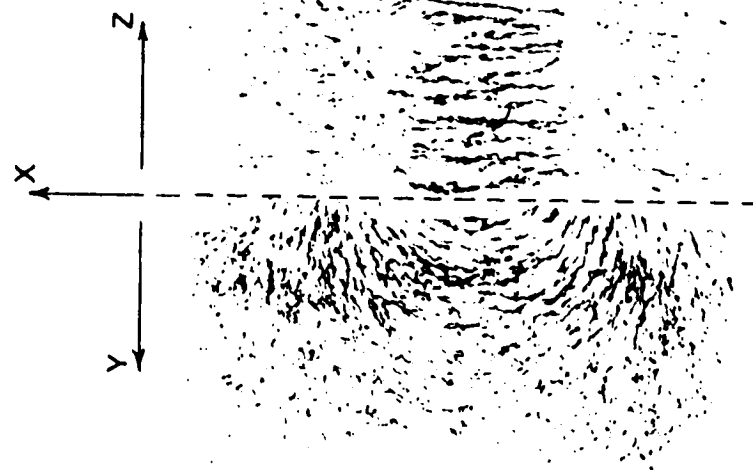


Figure 2.7. Magnetic field visualization.

ORIGINAL PAGE IS  
OF POOR QUALITY

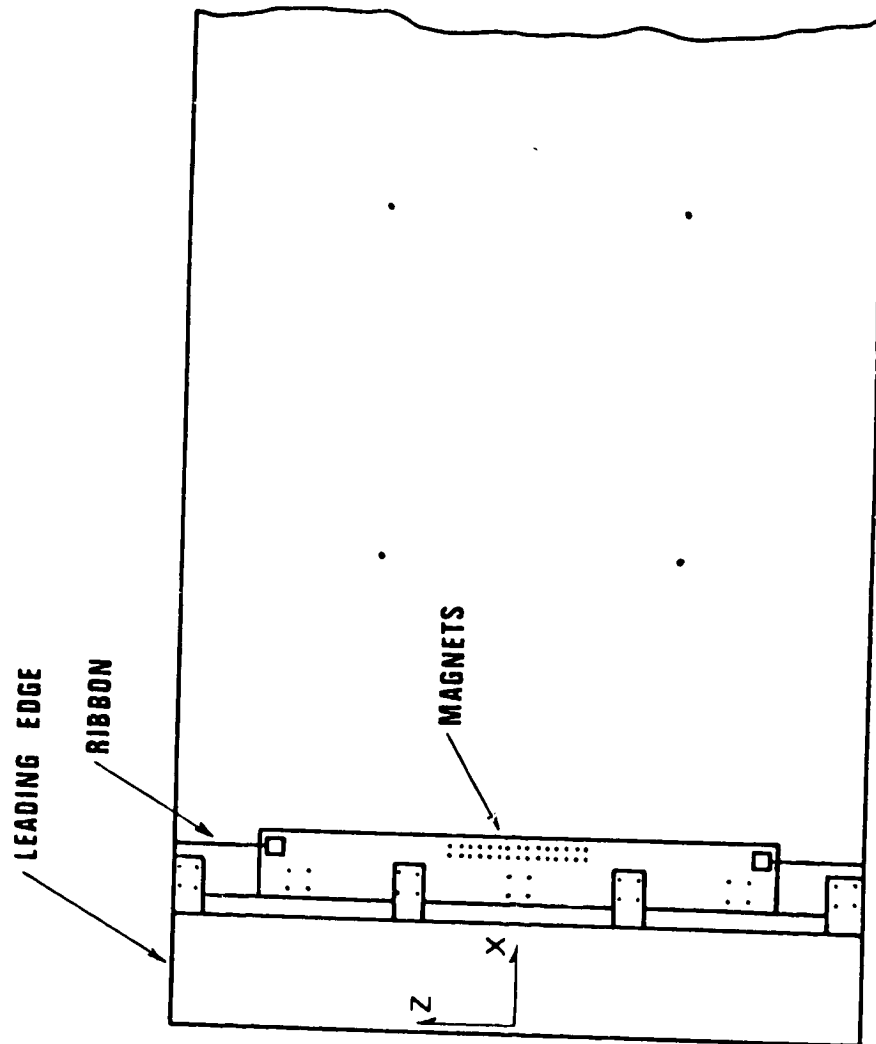


Figure 2.8 Electro-magnet configuration.

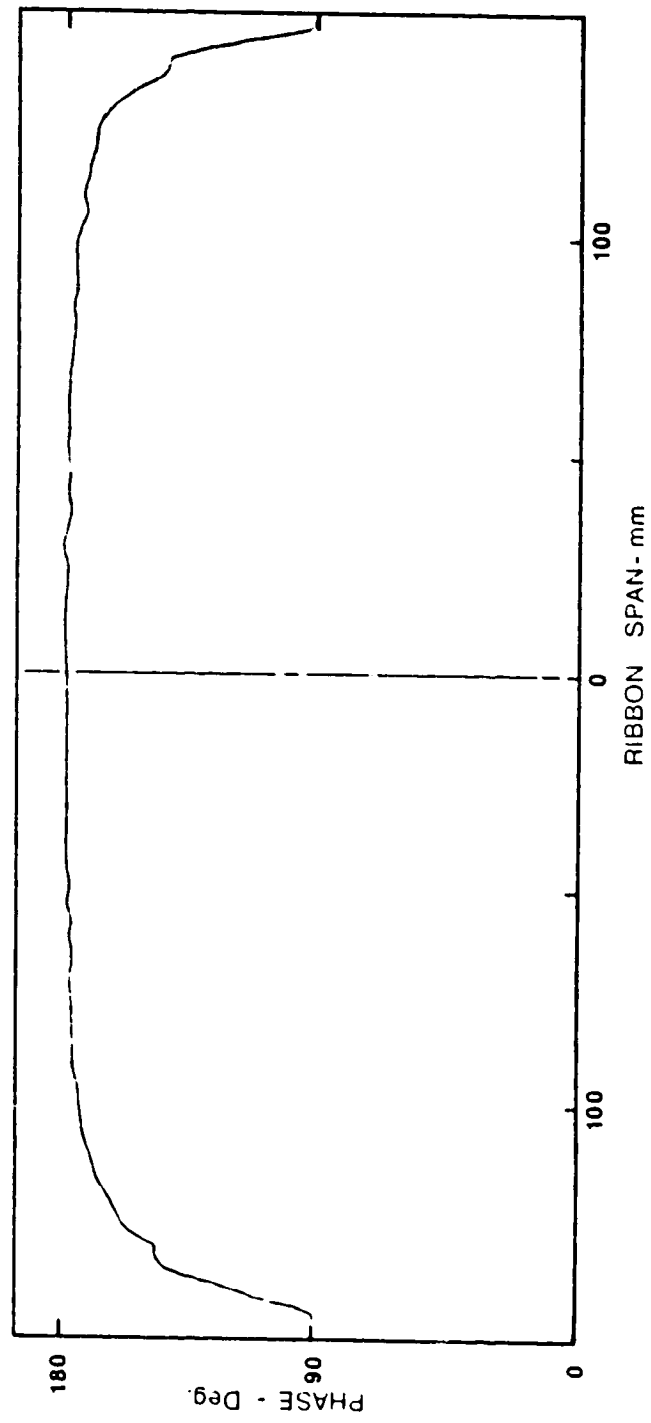


Figure 2.9 Spanwise phase distribution of the vibrating ribbon showing first-mode vibration.

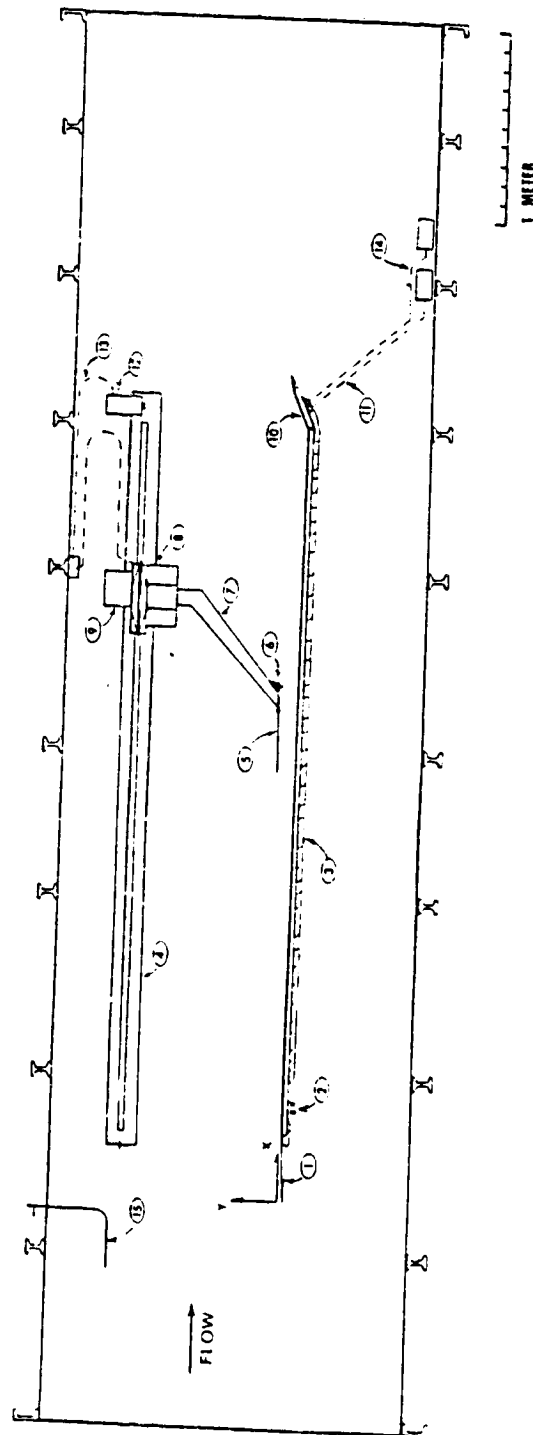


Figure 2.10 Test-section lay-out for experiments on the flat plate model using the 2-D traversing mechanism. The items noted are (1) Elliptical leading edge; (2) Electro-magnets for the vibrating ribbon; (3) Pressure port tubing bundles; (4) Support channel and guide rod for x-traverse; (5) Hot-wire probe extension tube; (6) Proximity probe; (7) Hot-wire probe sting; (8) 2-D traversing mechanism (9) Fairing for y-traverse stepping motor; (10) Trailing-edge flap; (11) Pressure port tubing bundles leave model on floor; (12) x-traverse stepping motor; (13) Stepping motor control cables; (14) scanivalves; (15) Pitot tube.

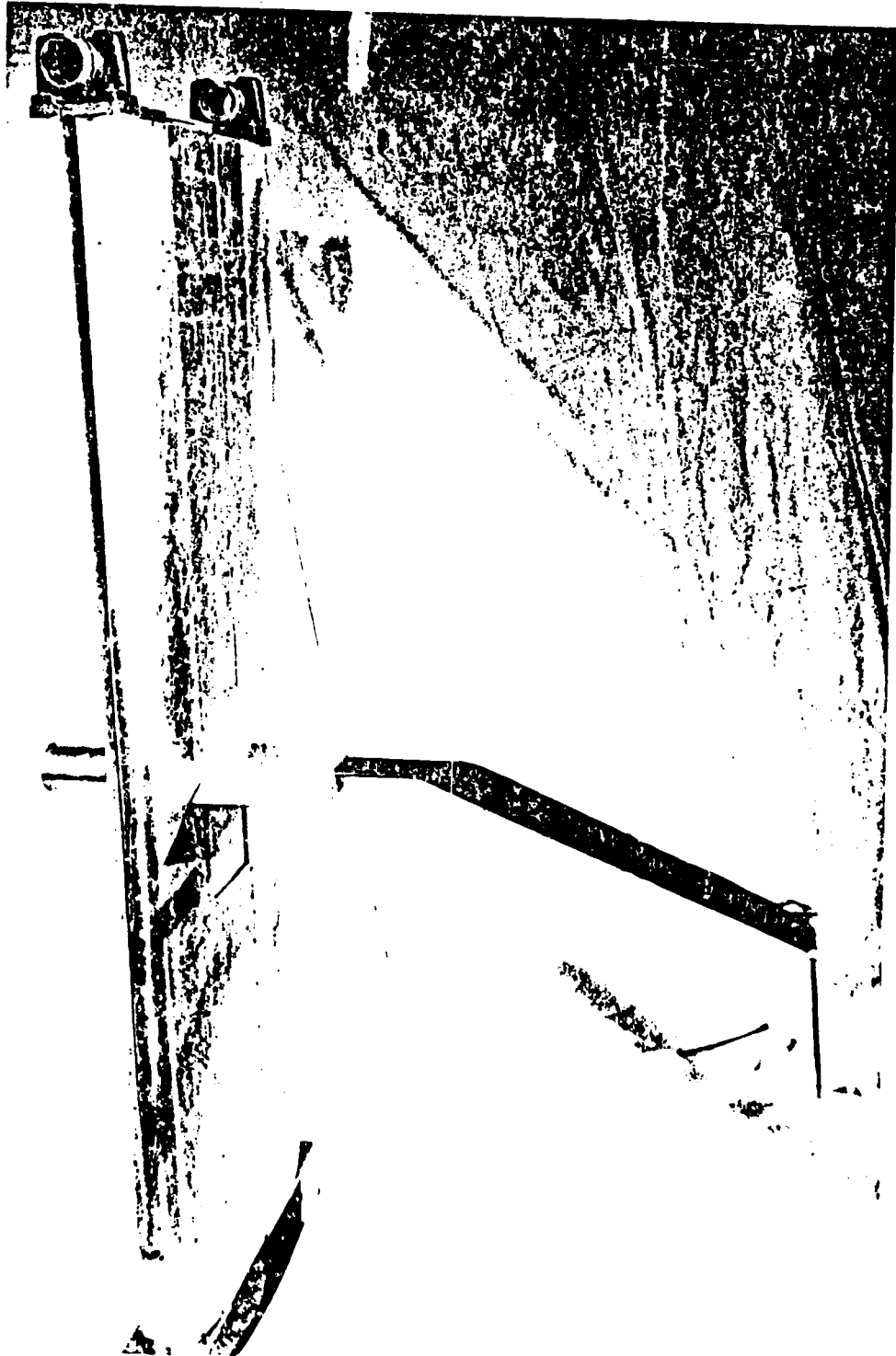


Figure 2.11. Three-dimensional traversing mechanism.

ORIGINAL PAGE IS  
OF POOR QUALITY

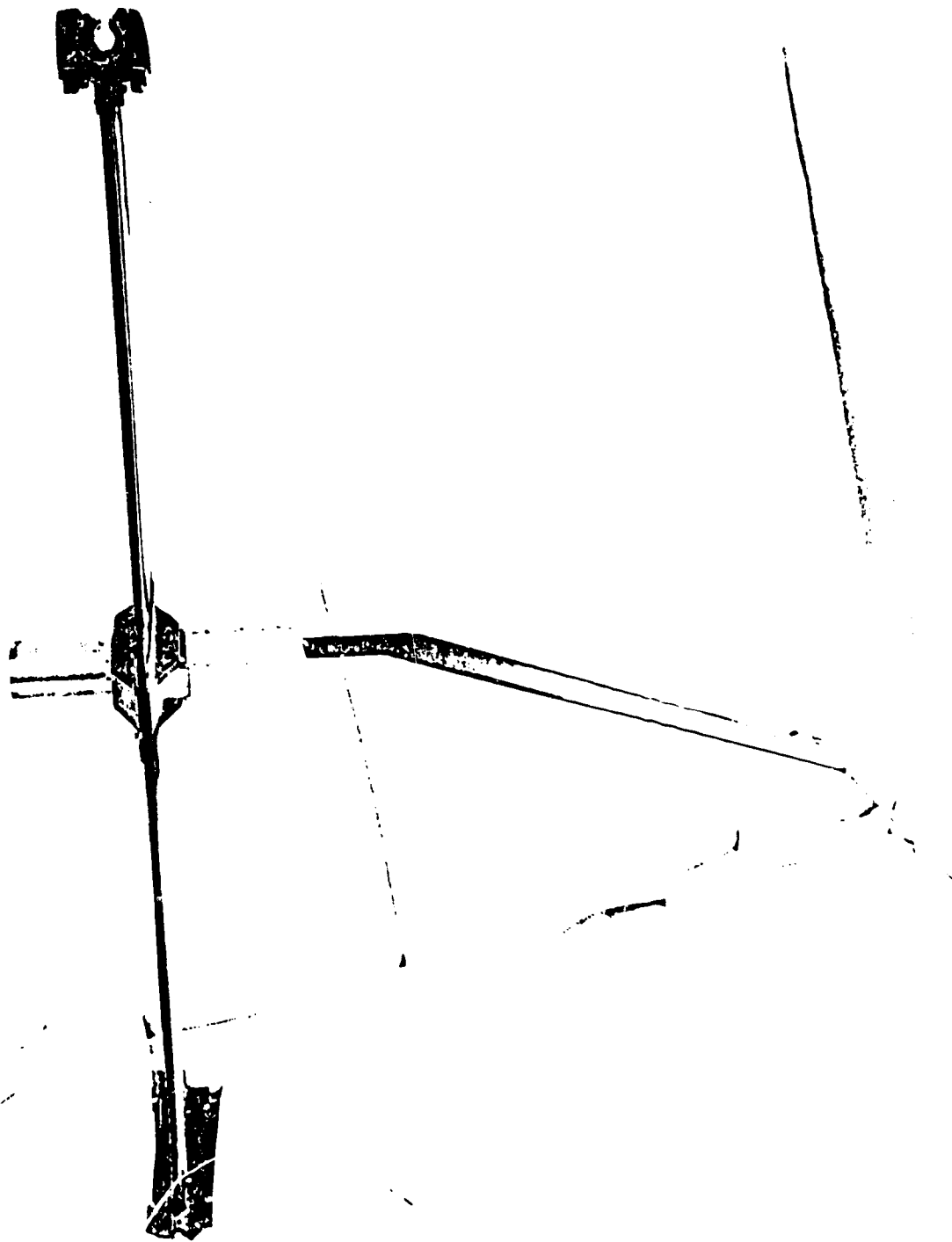


Figure 2.12. Two-dimensional traversing mechanism.

ORIGINAL PAGE IS  
OF POOR QUALITY

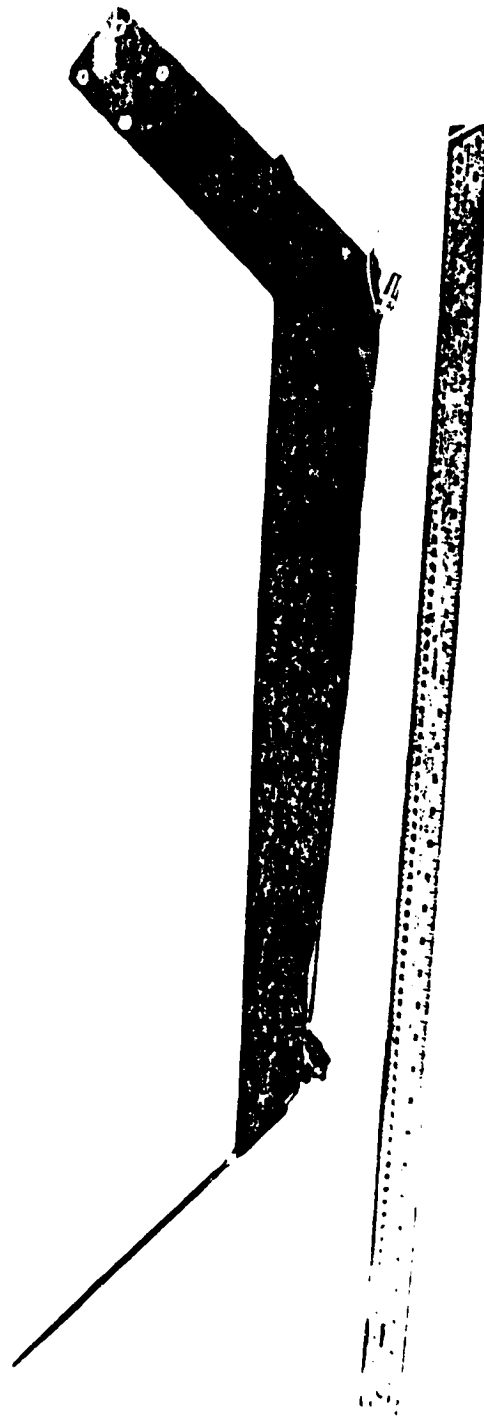


Figure 2.13. Traversing mechanism sting.



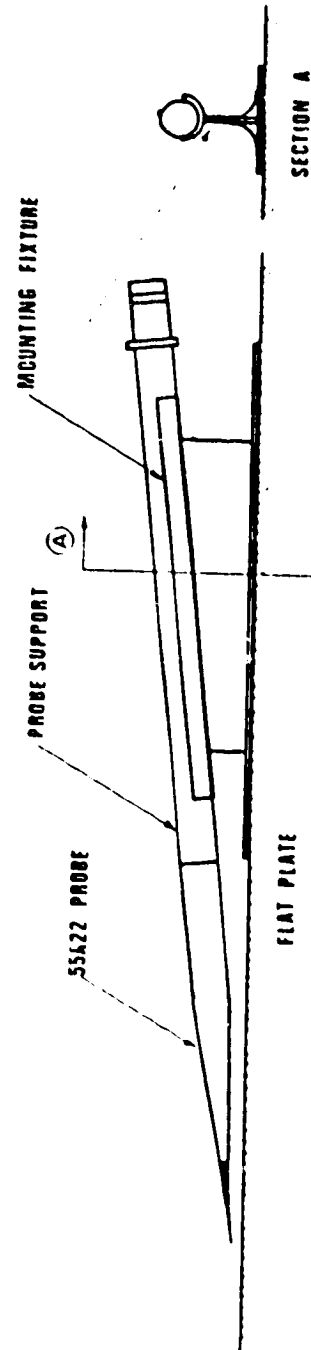


Figure 2.14 Fixed probe mount and DISA 55A22 probe.

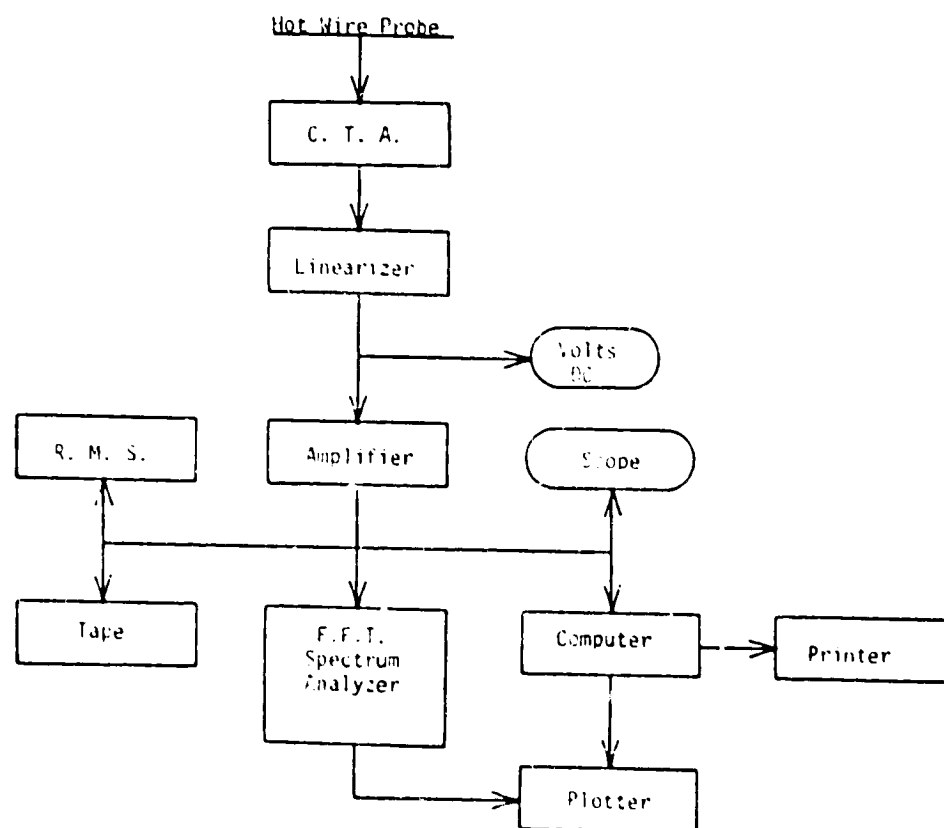


Figure 3.1 Schematic of the hot-wire anemometer signal processing.

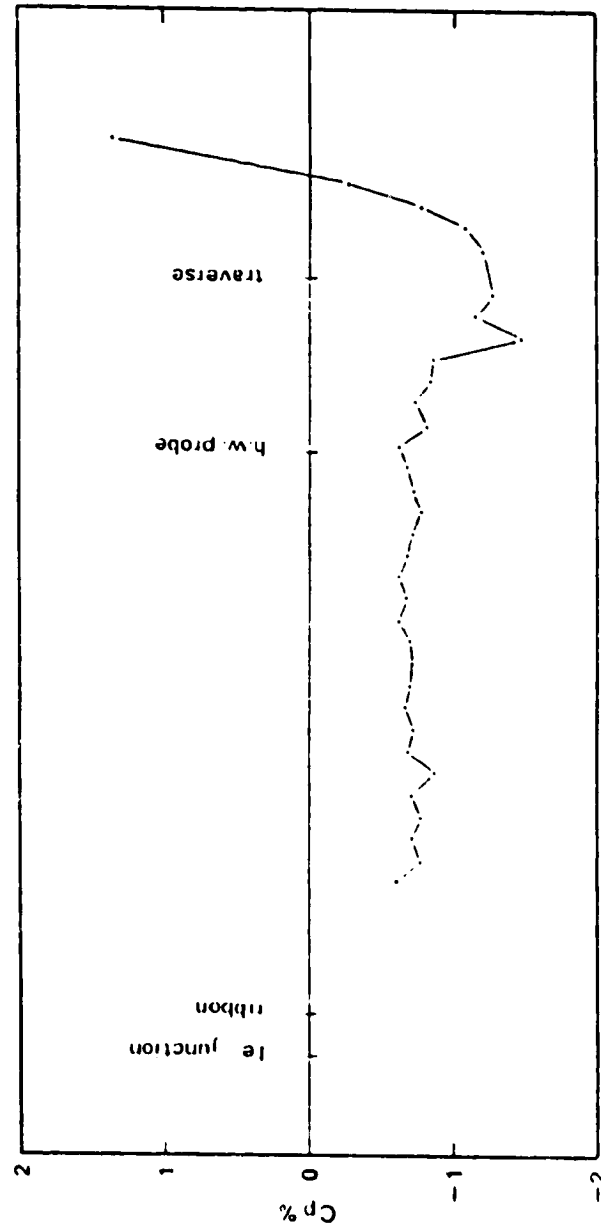


Figure 3.2 Chordwise pressure gradient showing zero pressure gradient at the hot-wire probe.

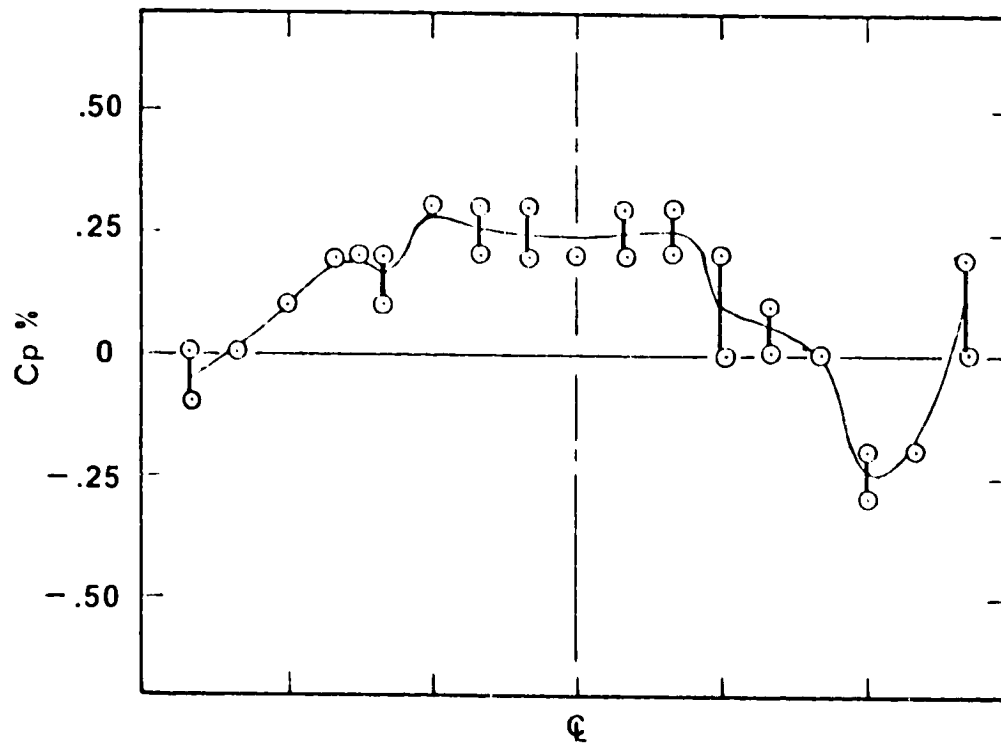


Figure 3.3 Spanwise pressure gradient. Connected data points denote variation in the data for the same flow conditions.

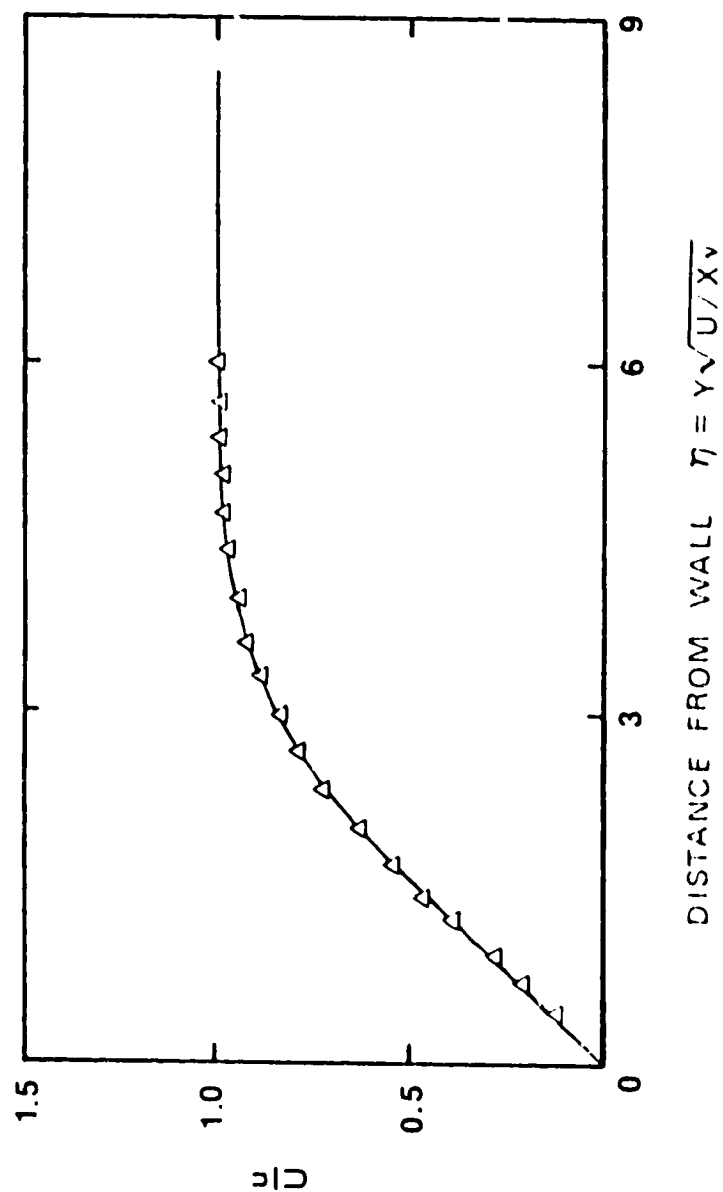


Figure 3.4 Measurement of boundary-layer mean velocity profile compared to the Blasius similarity solution.

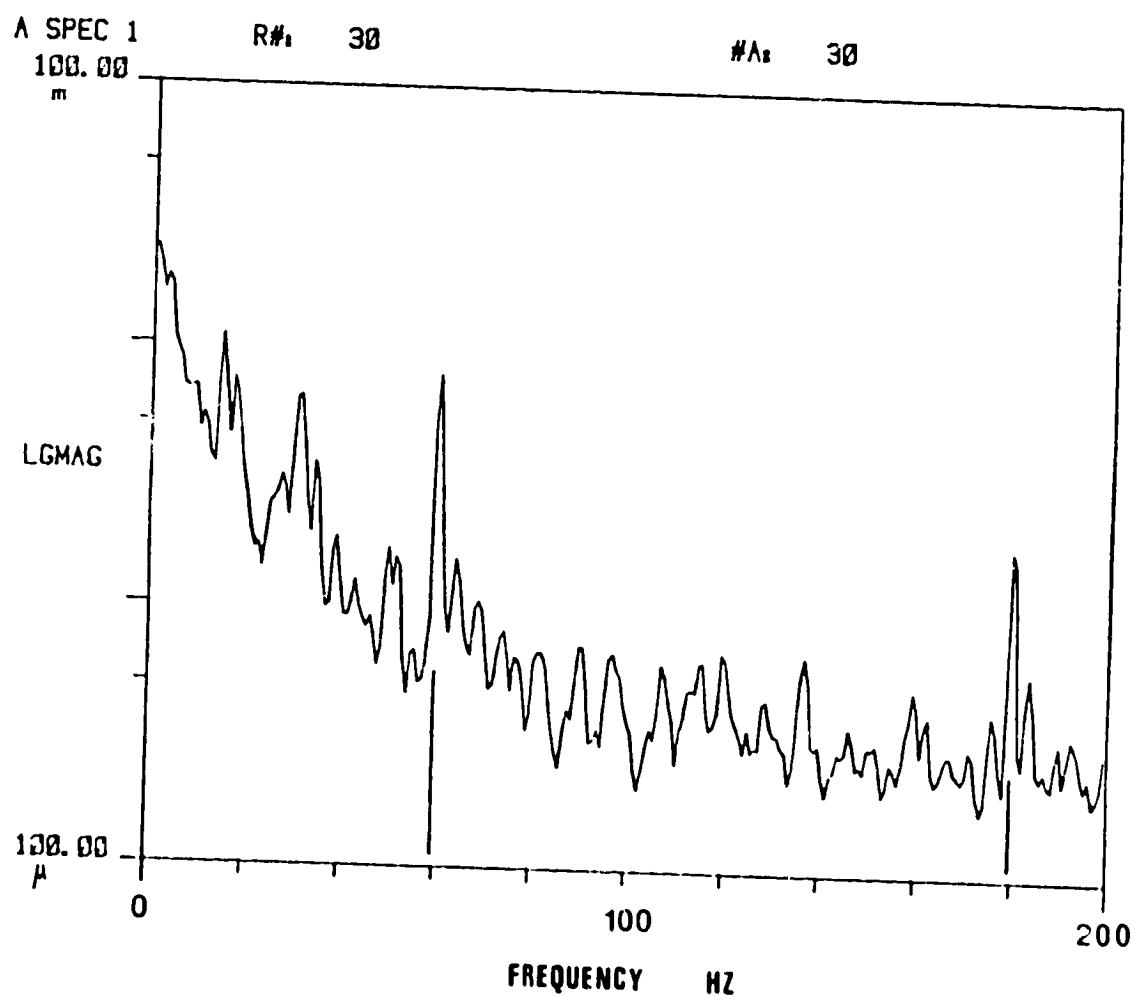


Figure 3.5 Free-stream turbulence spectra showing energy concentrated at the lower frequencies. The peaks at 60 Hz and 180 Hz are due to the a.c. line noise.

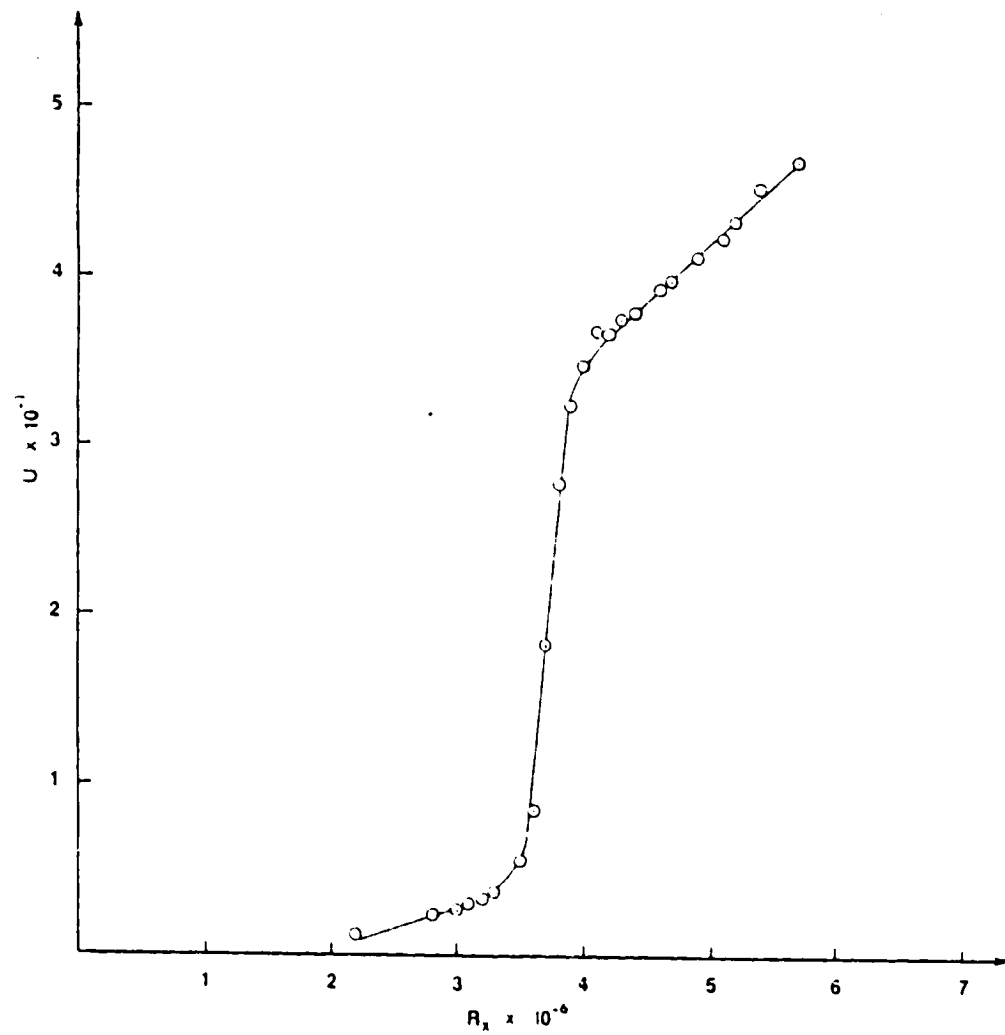


Figure 3.6 Transition Reynolds number obtained by plotting the mean boundary-layer velocity from the fixed probe vs. the free-stream Reynolds number. Transition begins at  $R \approx 3.5 \times 10^6$ .

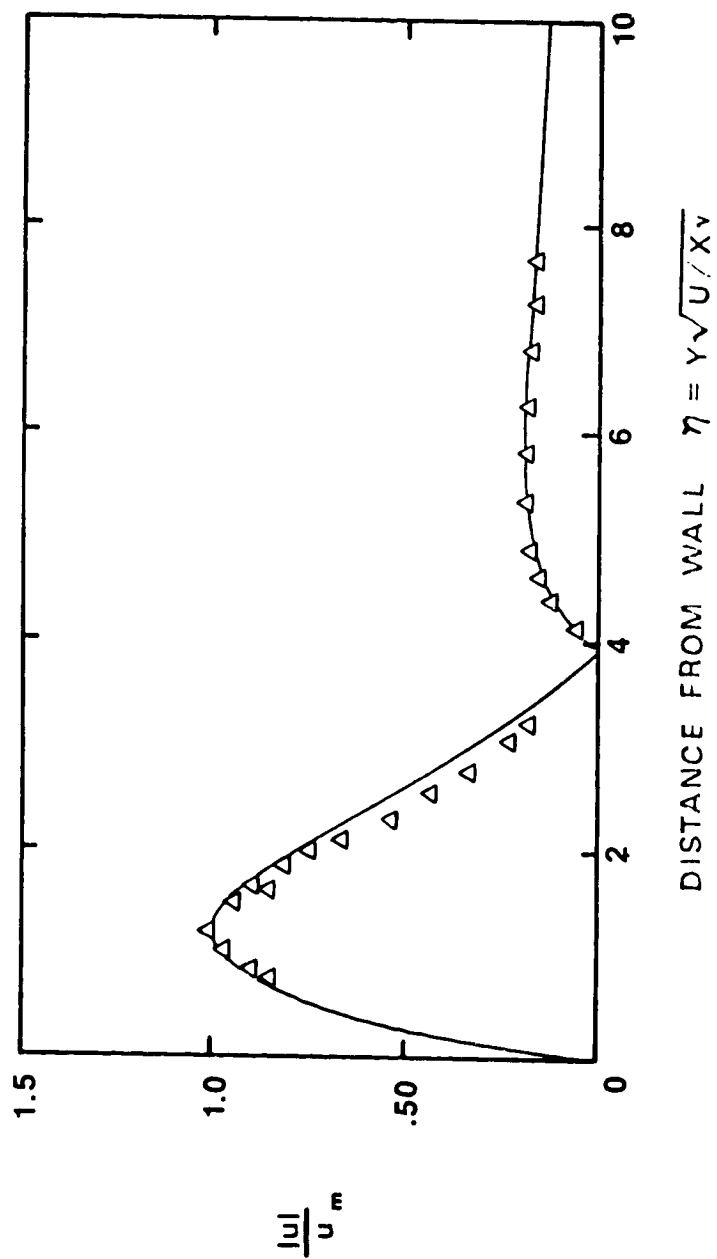


Figure 3.7 Measurements of the r.m.s. disturbance amplitude,  $|u|$ , compared with parallel theory predictions at  $F = 52 \times 10^{-6}$ ,  $R = 625$ .



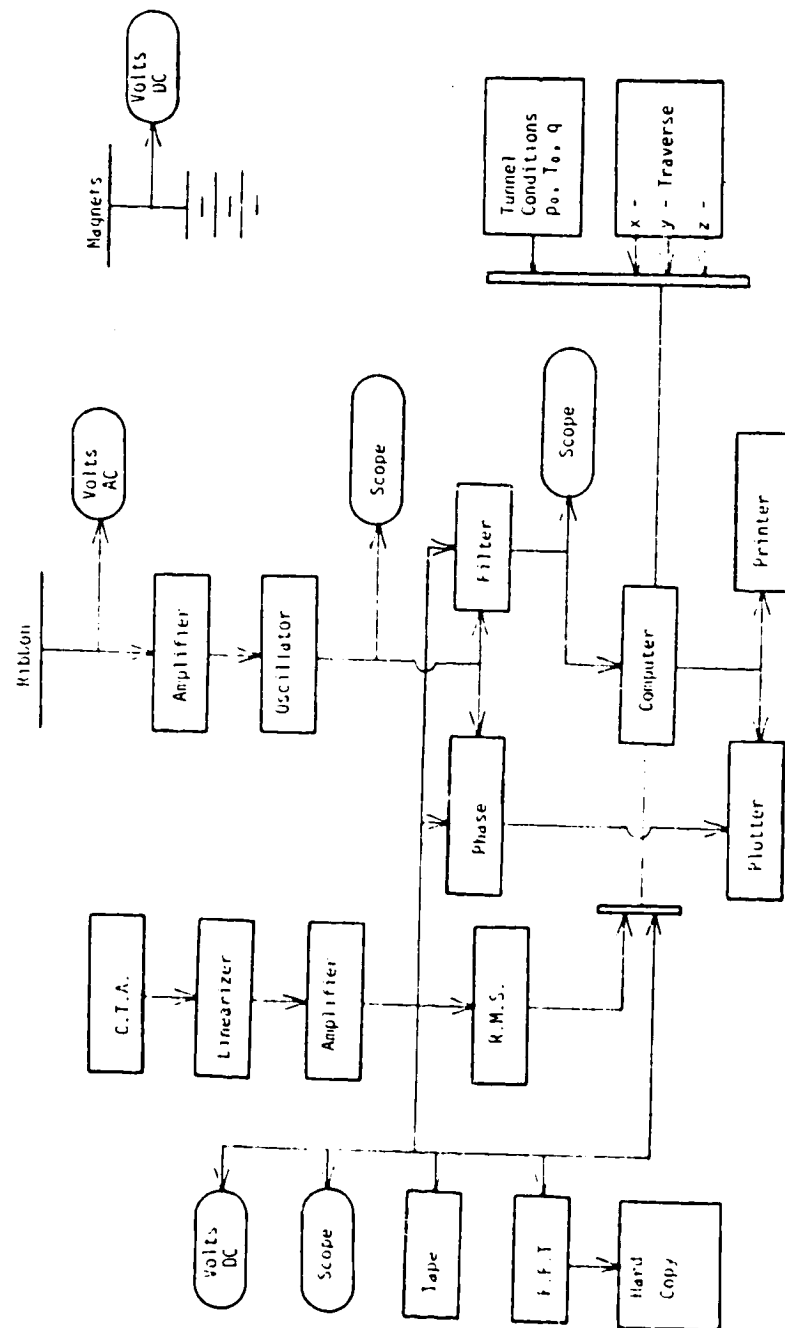


Figure 3.8 Schematic of electronics for signal processing of T-S waves.

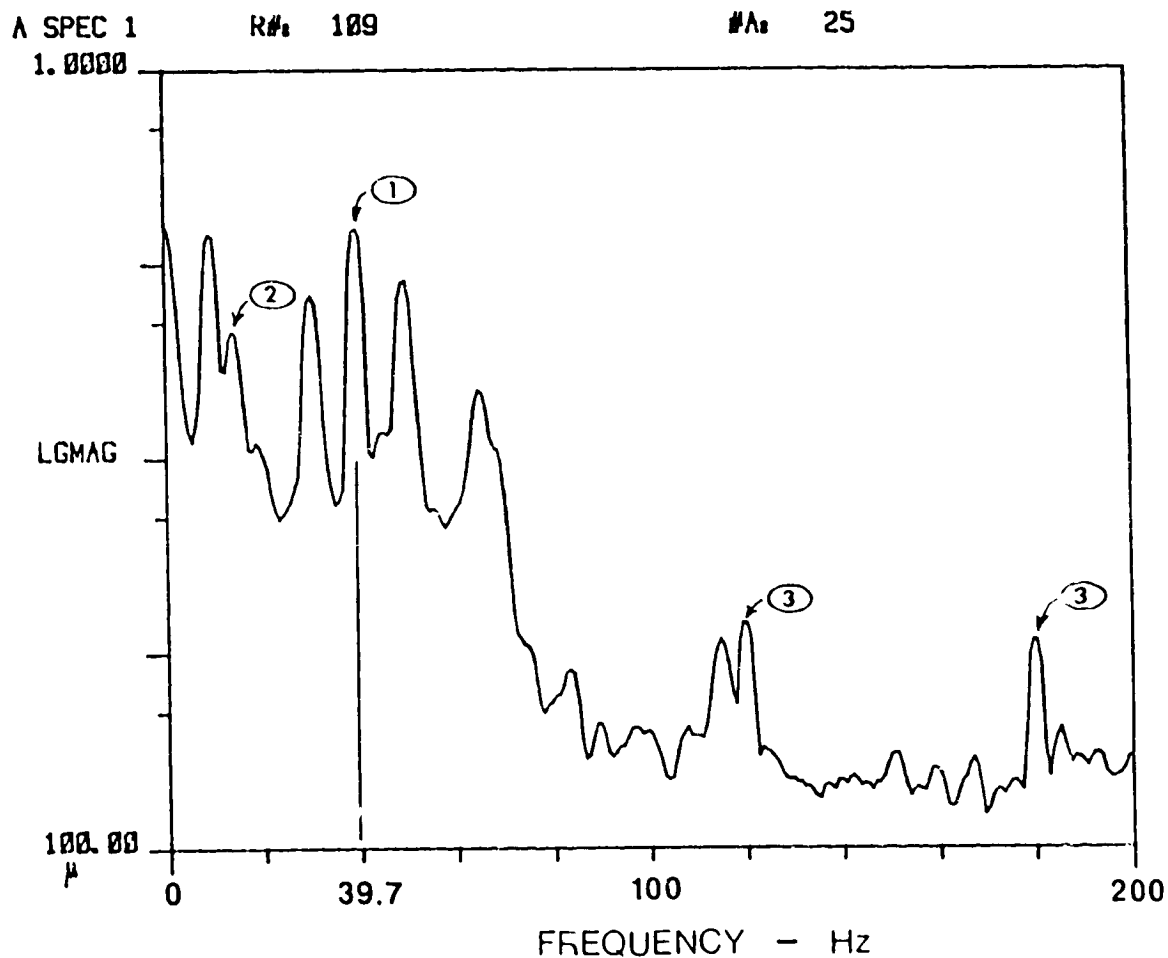


Figure 3.9 Hot-wire anemometer output spectral density at  $x = x_c$  in the boundary layer, showing

- (1) T-S wave at 39.7 Hz and  $u_{\eta}/U_{\infty} = 0.04\%$ .
- (2) probe vibration at  $\sim 14$  Hz due to motor-generator
- (3) electronic noise at 120 Hz and 180 Hz.

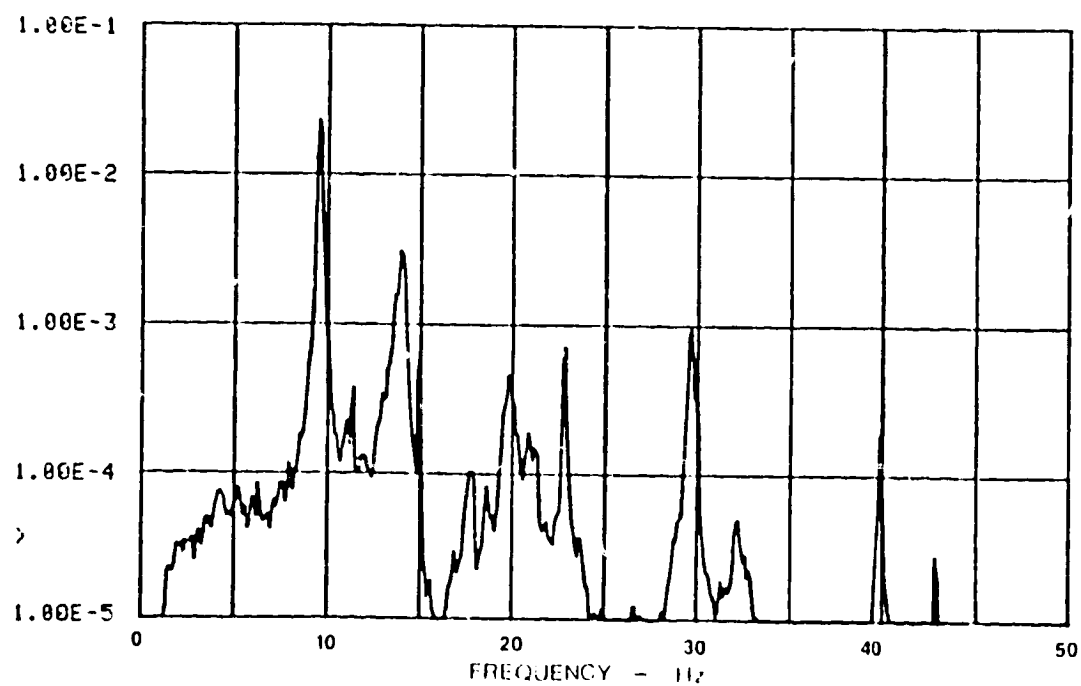


Figure 3.10 Spectral density of traverse vibration showing vibrational components of the hot-wire signal (Figure 3.9).

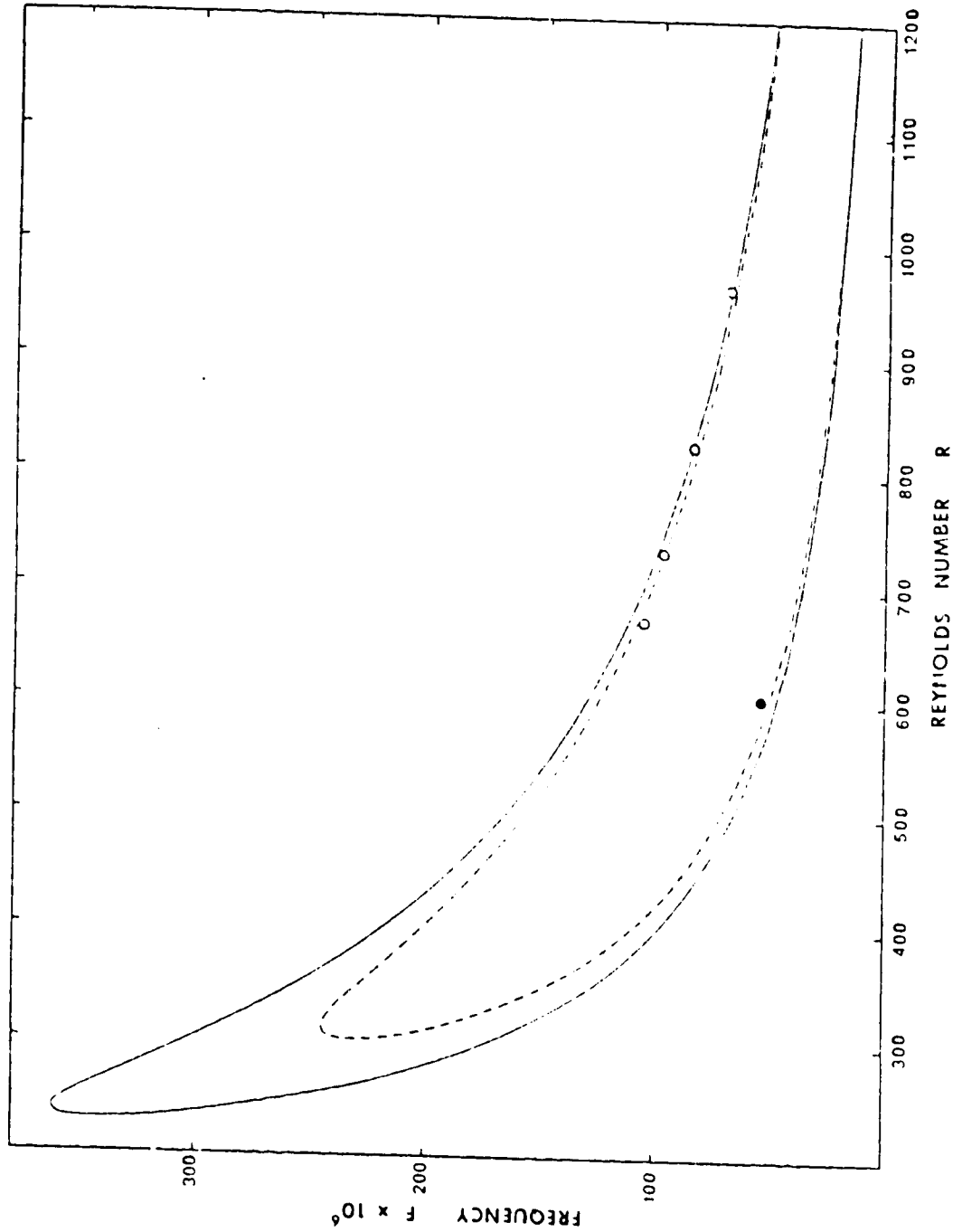


Figure 3.11 Neutral stability curve showing the present results obtained by measuring changes in  $u_{\max}$ . Solid symbols are branch I. Open symbols are branch II.

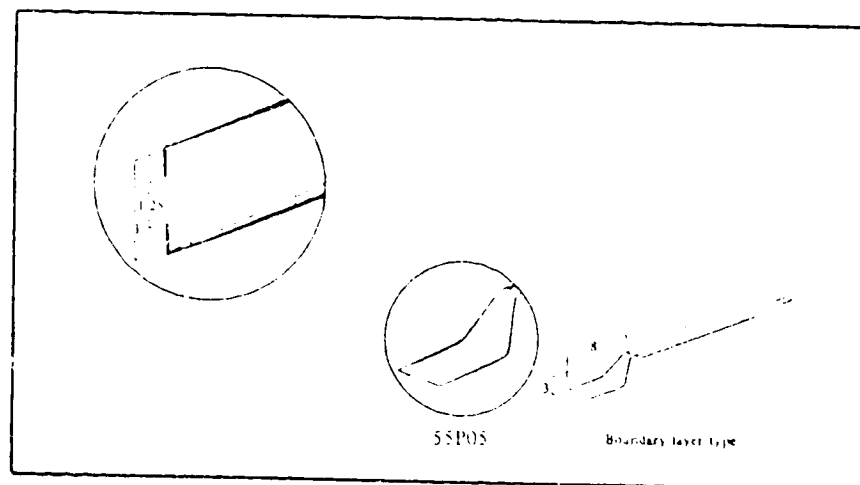
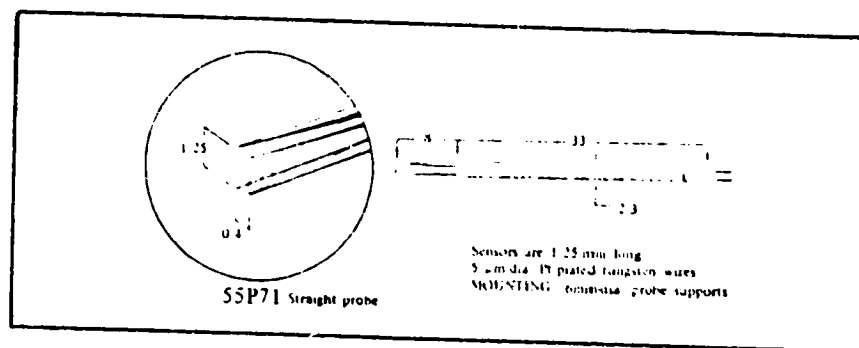


Figure A.1 DISA 55P05 Boundary-Layer Probe.



ORIGINAL PAGE IS  
OF POOR QUALITY

Figure A.2 DISA 55P71 Parallel-Array Turbulence Probe.

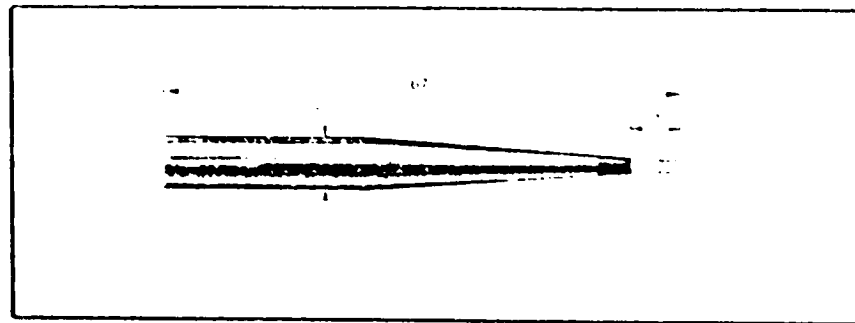


Figure A.3 DISA 55A22 General Purpose Hot-Wire Probe.

**END  
DATE  
FILMED**

SEP 12 1979